BEILSTEIN JOURNAL OF ORGANIC CHEMISTRY

Supporting Information

for

Sulfated prism[6]arene binds one guest internally and one guest externally

Emmanuel A. Bazan-Bergamino, Steven Ayoub, David L. Mobley and Lyle Isaacs

Beilstein J. Org. Chem. **2026,** *22,* 1635–1648. doi:10.3762/bjoc.22.132

Experimental materials, methods, and procedures, copies of ^{1}H, ^{13}C NMR, and DOSY spectra, ITC thermograms and coordinates from molecular modelling

License and Terms: This is a supporting information file under the terms of the Creative Commons Attribution License (https://creativecommons.org/licenses/by/4.0). Please note that the reuse, redistribution and reproduction in particular requires that the author(s) and source are credited and that individual graphics may be subject to special legal provisions.
The license is subject to the *Beilstein Journal of Organic Chemistry* terms and conditions: (https://www.beilstein-journals.org/bjoc/terms)

Table of contents **pages**

General experimental details ……... S2

Electronic supporting data availability statement …… S2

Synthetic procedure and characterization data for Pr[6]AS …… S2–S5

Variable temperature ^{1}H NMR spectra for Pr[6]AS ……. S6

^{1}H NMR dilution experiment for Pr[6]AS …….. S7–S8

^{1}H NMR stack plots for selected guests with Pr[6]AS ……...…… S9–S22

Isothermal titration calorimetry (ITC) experiments …… S23–S28

Supplementary MD figures ……..……..…….. S29–S34

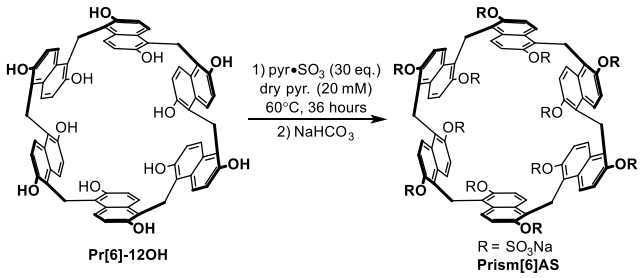
Computational methods …… S35–S38

References …… S39–S41

General experimental details.
All starting materials and solvents were purchased as reagent grade and used without further purification unless otherwise stated. $(HO)_{12}$Pr[6]arene was synthesized according to the procedures by Gaeta.[1] NMR spectra were measured on a Bruker 600 MHz spectrometer at 25 °C unless otherwise indicated. ITC data were measured on a Malvern Microcal PEAQ-ITC instrument. Routine mass spectrometry was performed using a JEOL AccuTOF electrospray ionization (ESI) instrument.

Electronic supporting data availability. The electronic data that support this publication can be freely downloaded from the Digital Repository at the University of Maryland (https://drum.lib.umd.edu/home) via the following doi:10.13016/s4v4-dkcq. The electronic data from the molecular dynamics simulations can be accessed at the following doi:10.5281/zenodo.23380489.

Synthetic procedures and characterization data



Pr[6]AS. A 4 mL vial was charged with a stirring bar and $(HO)_{12}$Pr[6]arene (30 mg, 0.029 mmol, 1.0 equiv) and then capped with a septum. The vial was then subjected to high vacuum at 40 °C for 20 minutes and backfilled with nitrogen (3×). Pyridine·sulfur trioxide complex (140 mg, 0.871 mmol, 30 equiv) was added and evacuated once again for 10 minutes, then backfilled with nitrogen. Under nitrogen flow, dry pyridine (1.5 mL) was added to the vial. The vial was capped tightly and the mixture stirred at 60 °C for 36 hours. The reaction mixture was cooled to room temperature and the pyridine supernatant was removed by syringe. Deionized water (1.0 mL) was added to the precipitate which formed a solution. Next, a saturated aq. solution of sodium bicarbonate was added to raise the pH from 5 to 8 (monitored using pH strips). The resulting solution was concentrated by rotary evaporation (40 °C) to remove water and pyridine. Then, a small amount of deionized water (1.0 mL) was added and the solution was concentrated by rotary evaporation followed by drying at high vacuum overnight to completely remove pyridine. The resulting solid was dissolved in DI water (400 µL) and transferred to a 1.5 mL centrifuge tube by micropipette. Acetone (800 µL) was added to the solution and the resulting mixture was vortexed and left to settle for 10 minutes to produce a white solid precipitate. The tube was centrifugated (8,000 rpm × 5 min) and the supernatant was transferred by micropipette to a 4 mL vial then dried by rotary evaporation to remove water and acetone. This 1:2 water/acetone separation process was repeated two more times with less water each time (250 µL then 150 µL) to collect more product after drying. The solid was dissolved in water (1 mL) and lyophilized to obtain Pr[6]AS (22 mg, 35% yield, 75% content) as a light orange solid. M.p.: > 240 ˚C (dec.). IR (ATR, cm^{-1}): 3475w, 1624w, 1599w, 1509w, 1441w, 1400w, 1228s, 1135m, 1056s, 1007s, 850m, 784s, 540m, 615s. ^{1}H NMR (600 MHz, 50 ˚C, D_2O) δ 7.95 (d, J = 8.8 Hz, 12H), 7.44 (d, J = 8.8 Hz, 12H), 4.91 (s, 12H). ^{13}C NMR (150 MHz, 25 ˚C, D_2O, $NaHCO_3$ as internal reference): δ 142.7, 127.6, 125.3, 121.0, 117.6, 20.4 ppm. ESI-MS (negative ion mode): *m/z* 718.87 ($[M - 8SO_3Na + 6H]^{2-}$), calc for $C_{66}H_{42}O_{24}S_4Na_4^{2-}$, 719.03.

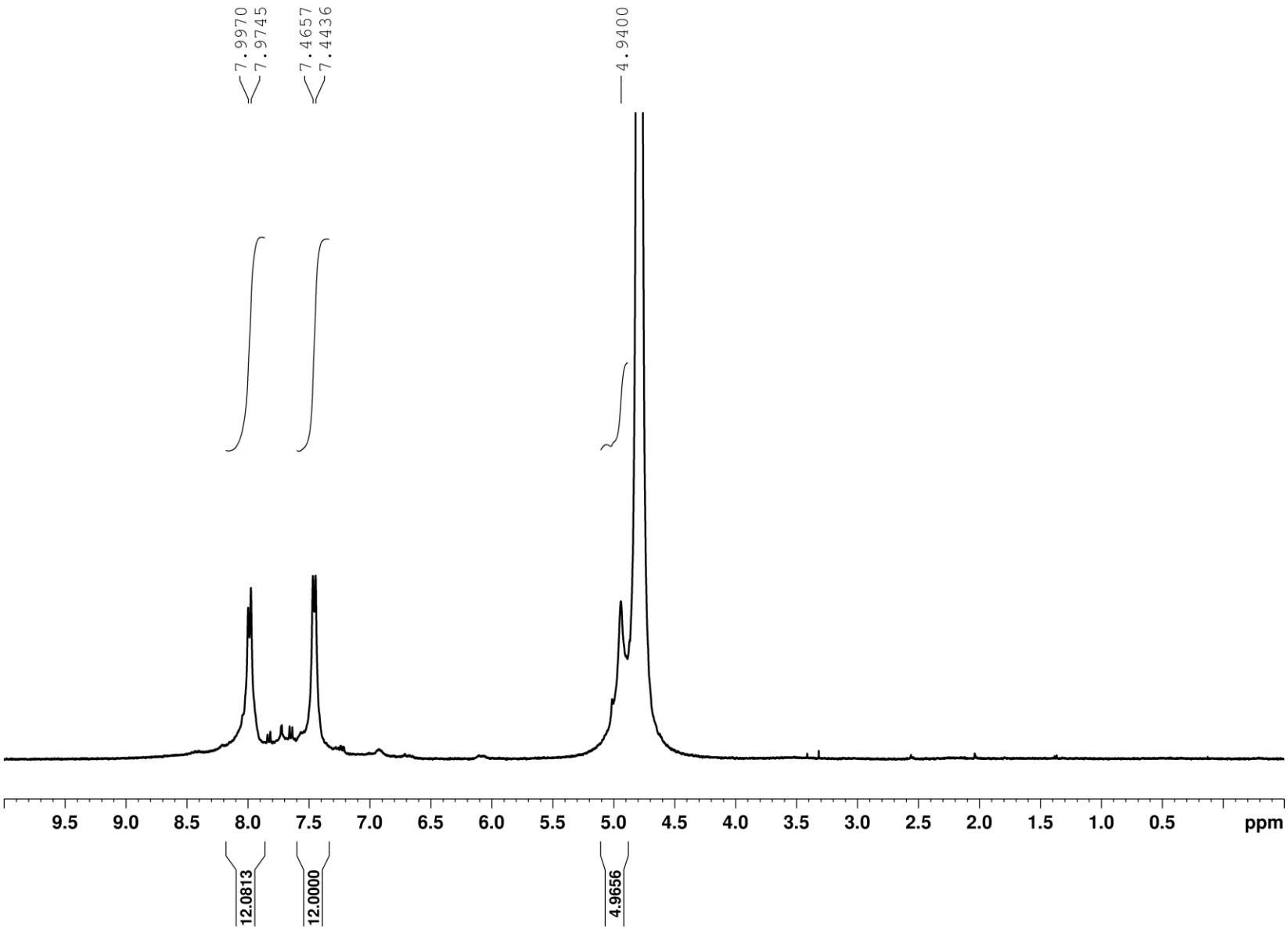


Figure S1. ^{1}H NMR spectrum recorded (600 MHz, 25 °C, D_2O) for Pr[6]AS.

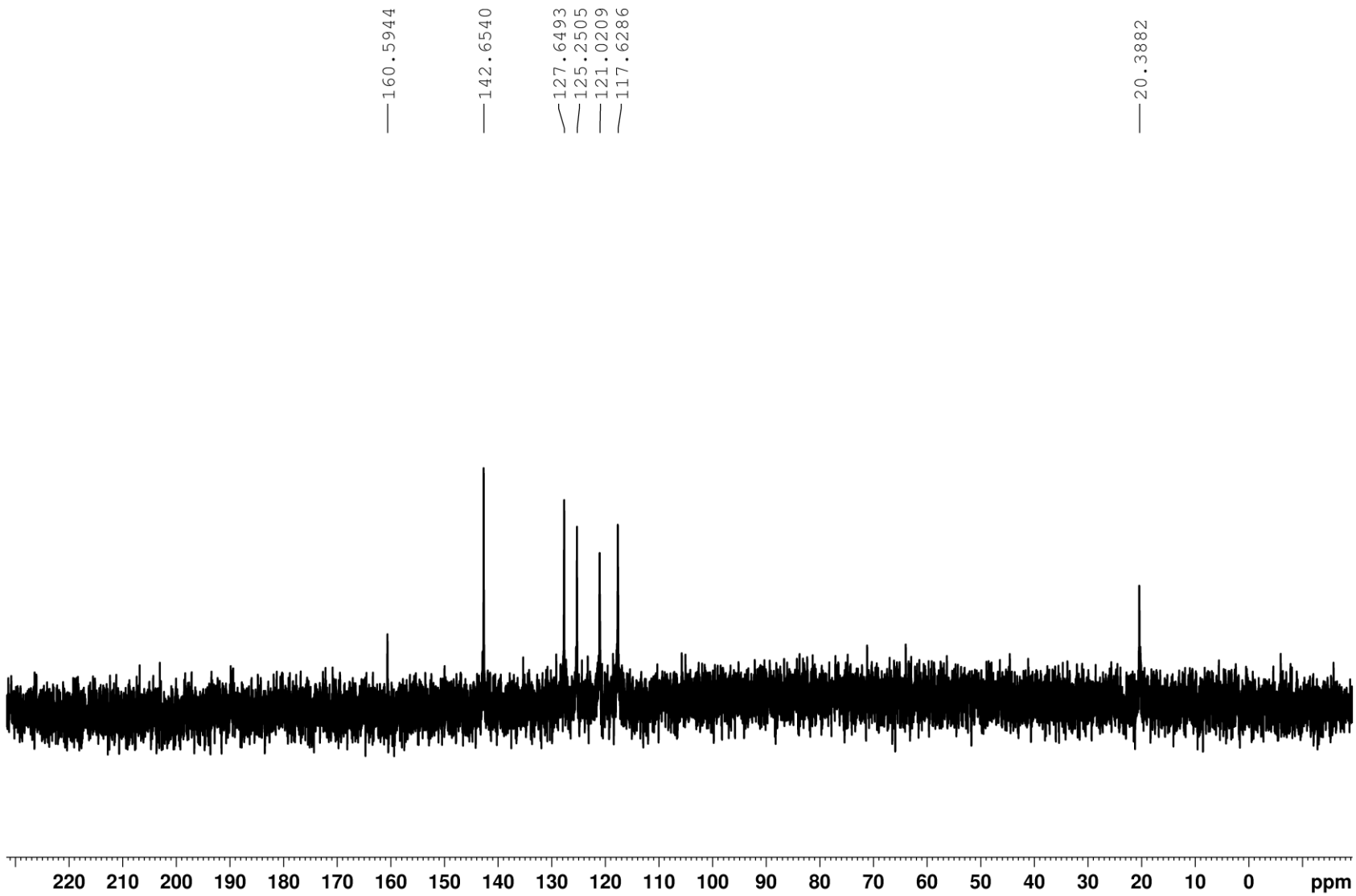


Figure S2. ^{13}C NMR spectrum recorded (150 MHz, 25 °C, D_2O, $NaHCO_3$ as internal standard) for Pr[6]AS. The resonance at 160.59 ppm arises from the internal standard ($NaHCO_3$).

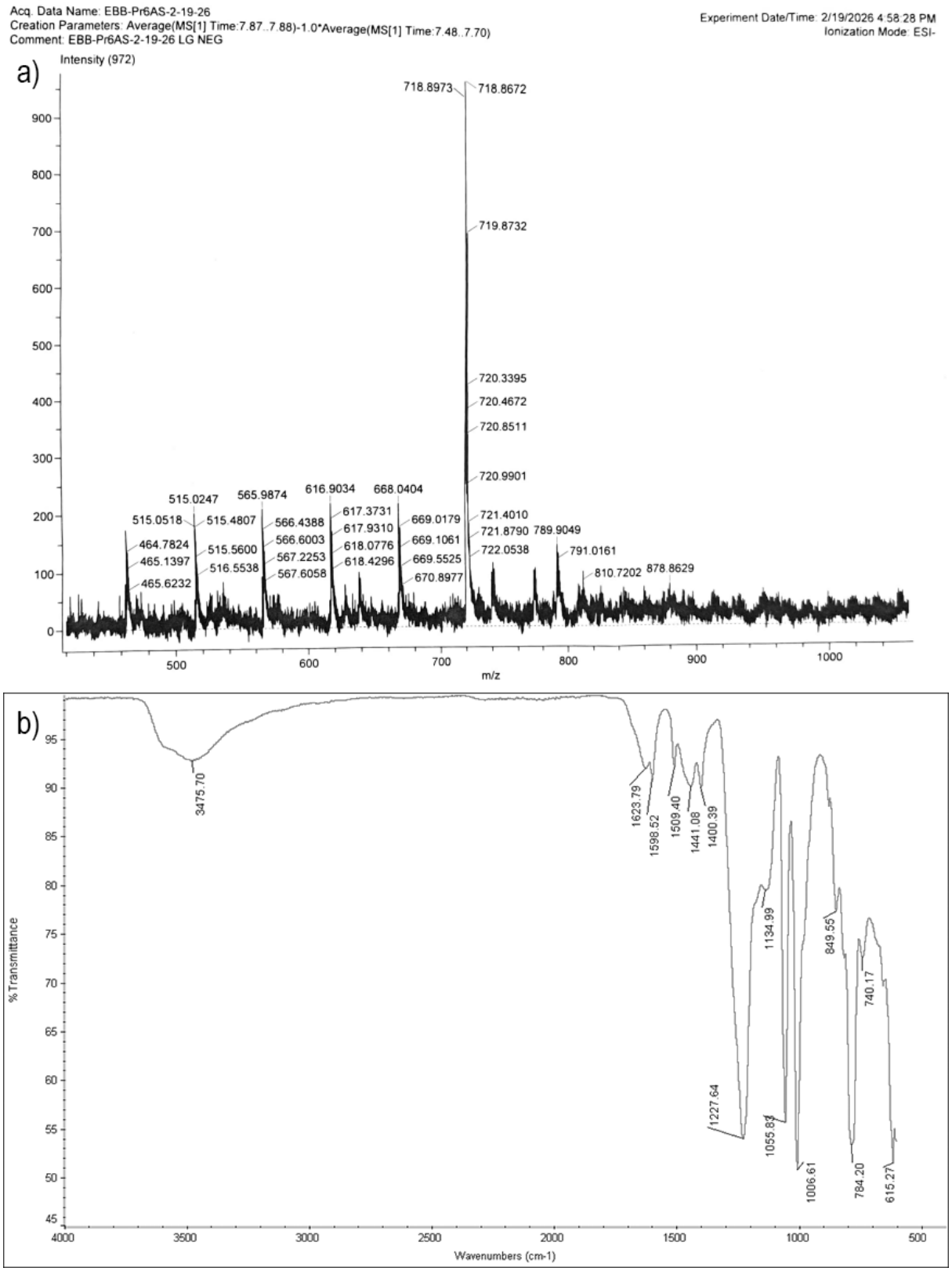


Figure S3. a) Mass spectrum (ESI, negative ion mode) recorded for Pr[6]AS. b) IR spectrum (ATR, cm^{-1}) recorded for Pr[6]AS.

Variable-temperature ^{1}H NMR spectra for Pr[6]AS

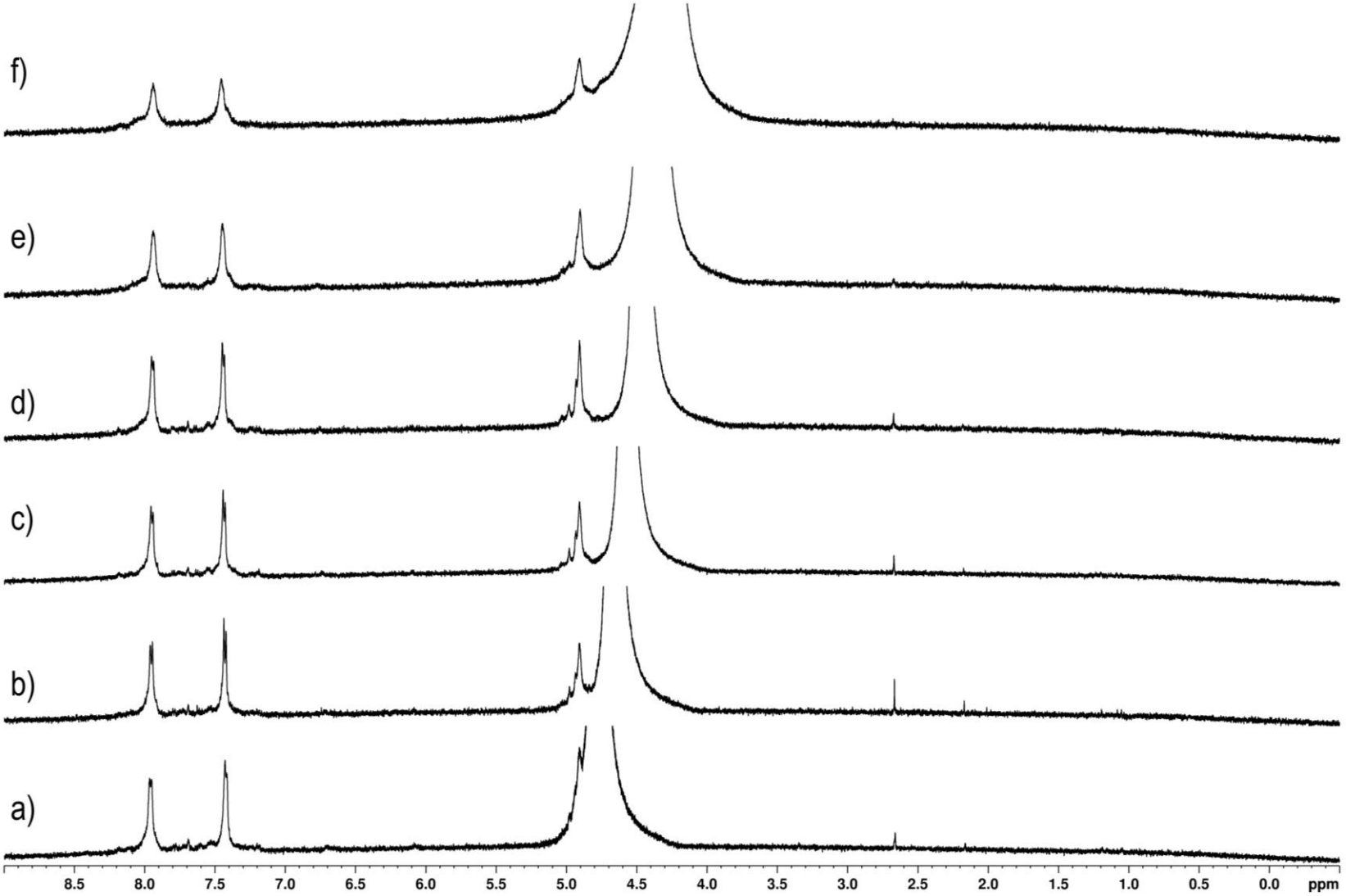


Figure S4. ^{1}H NMR spectra recorded (600 MHz, D_2O) for Pr[6]AS (0.5 mM) at different temperatures: a) 293 K, b) 303 K, c) 313 K, d) 323 K, e) 333 K, f) 343 K.

^{1}H NMR dilution experiment for Pr[6]AS

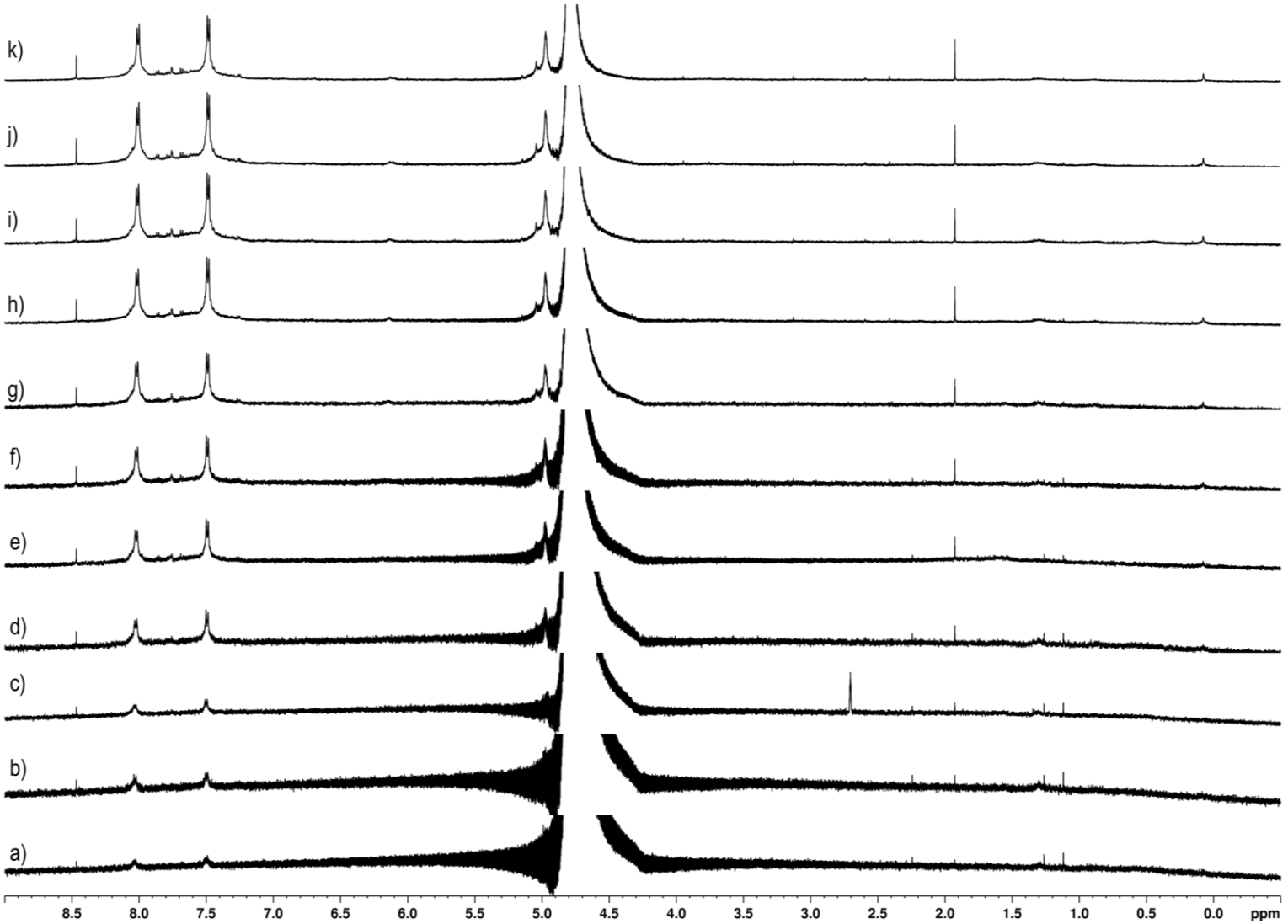


Figure S5. ^{1}H NMR spectra recorded (600 MHz, 25 °C, D_2O) for Pr[6]AS at different concentrations: a) 0.05 mM, b) 0.075 mM, c) 0.10 mM, d) 0.25 mM, e) 0.50 mM, f) 0.75 mM, g) 1.0 mM, h) 2.0 mM, i) 3.0 mM, j) 4.0 mM, k) 5.0 mM.

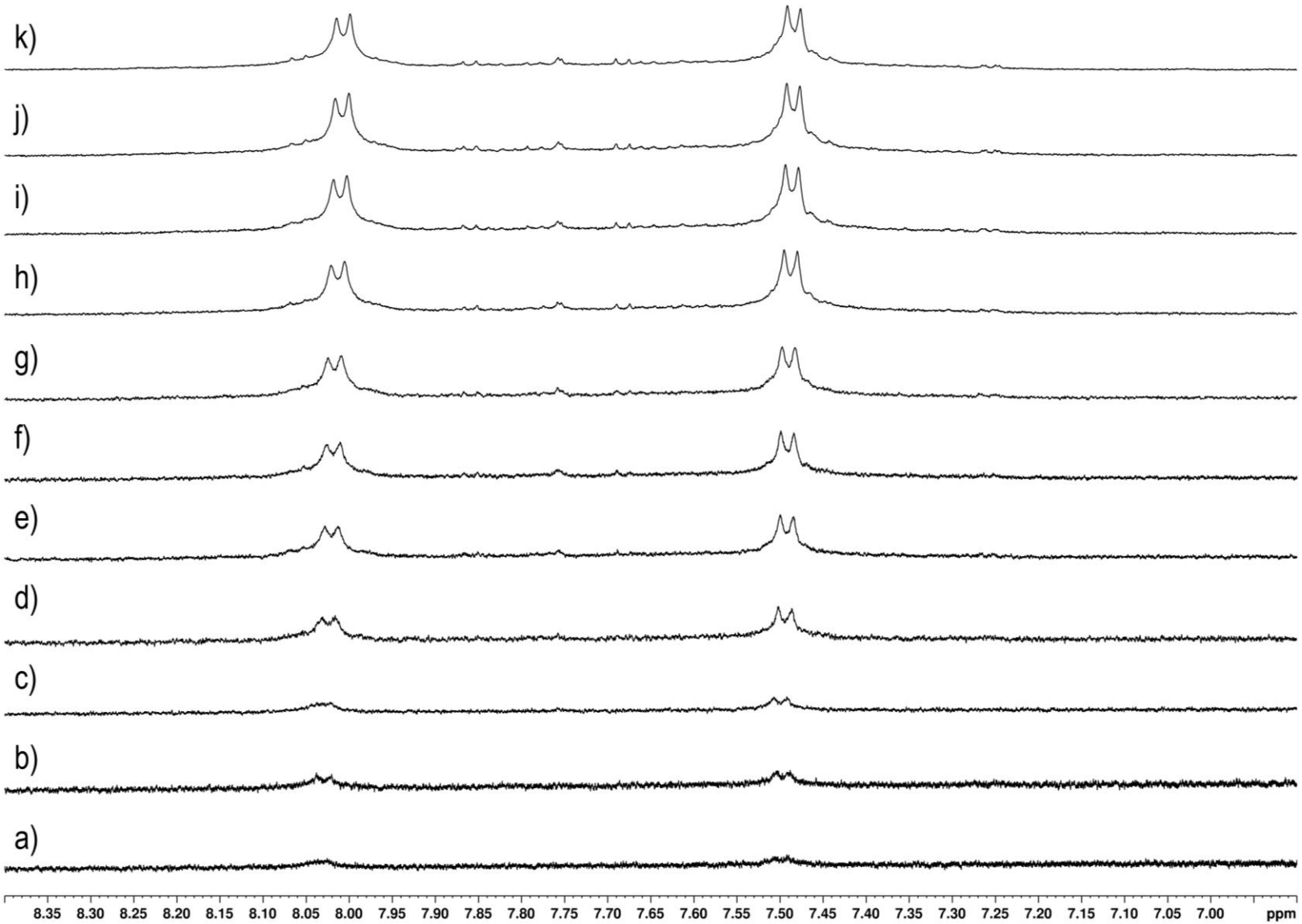


Figure S6. Zoomed in ^{1}H NMR spectra recorded (600 MHz, 25 °C, D_2O) for Pr[6]AS at different concentrations: a) 0.05 mM, b) 0.075 mM, c) 0.10 mM, d) 0.25 mM, e) 0.50 mM, f) 0.75 mM, g) 1.0 mM, h) 2.0 mM, i) 3.0 mM, j) 4.0 mM, k) 5.0 mM.

^{1}H NMR stack plots for selected guests with Pr[6]AS

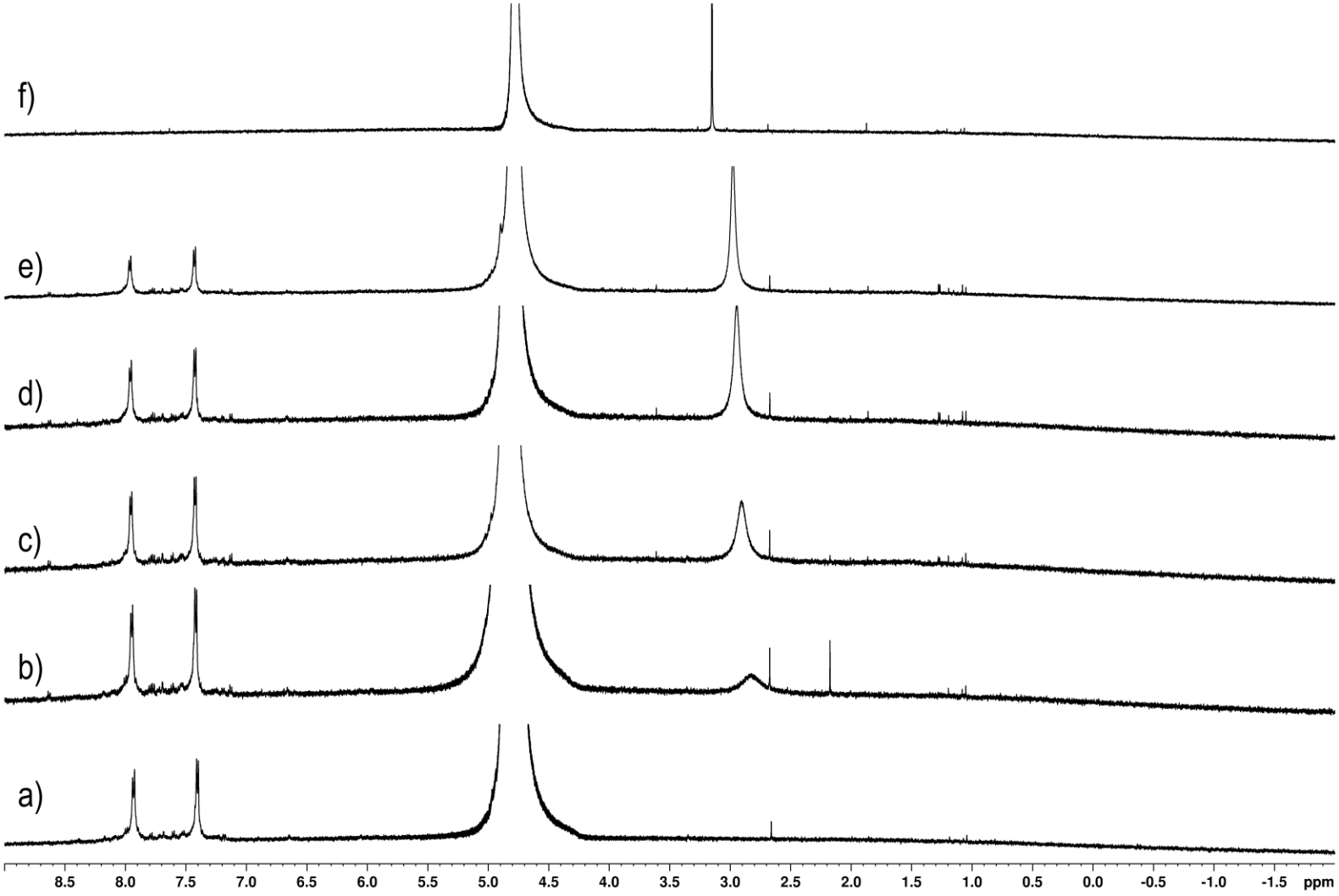


Figure S7. ^{1}H NMR spectra recorded (600 MHz, 25 °C, D_2O) for: a) Pr[6]AS (0.1 mM), b) an equimolar mixture of Pr[6]AS and **1** (NMe_4) (0.1 mM), c) a 1:2 mixture of Pr[6]AS (0.1 mM) and **1** (NMe_4) (0.2 mM), d) a 1:3 mixture of Pr[6]AS (0.1 mM) and **1** (NMe_4) (0.3 mM), e) a 1:4 mixture of Pr[6]AS (0.1 mM) and **1** (NMe_4) (0.4 mM), and f) **1** (NMe_4) (0.4 mM).

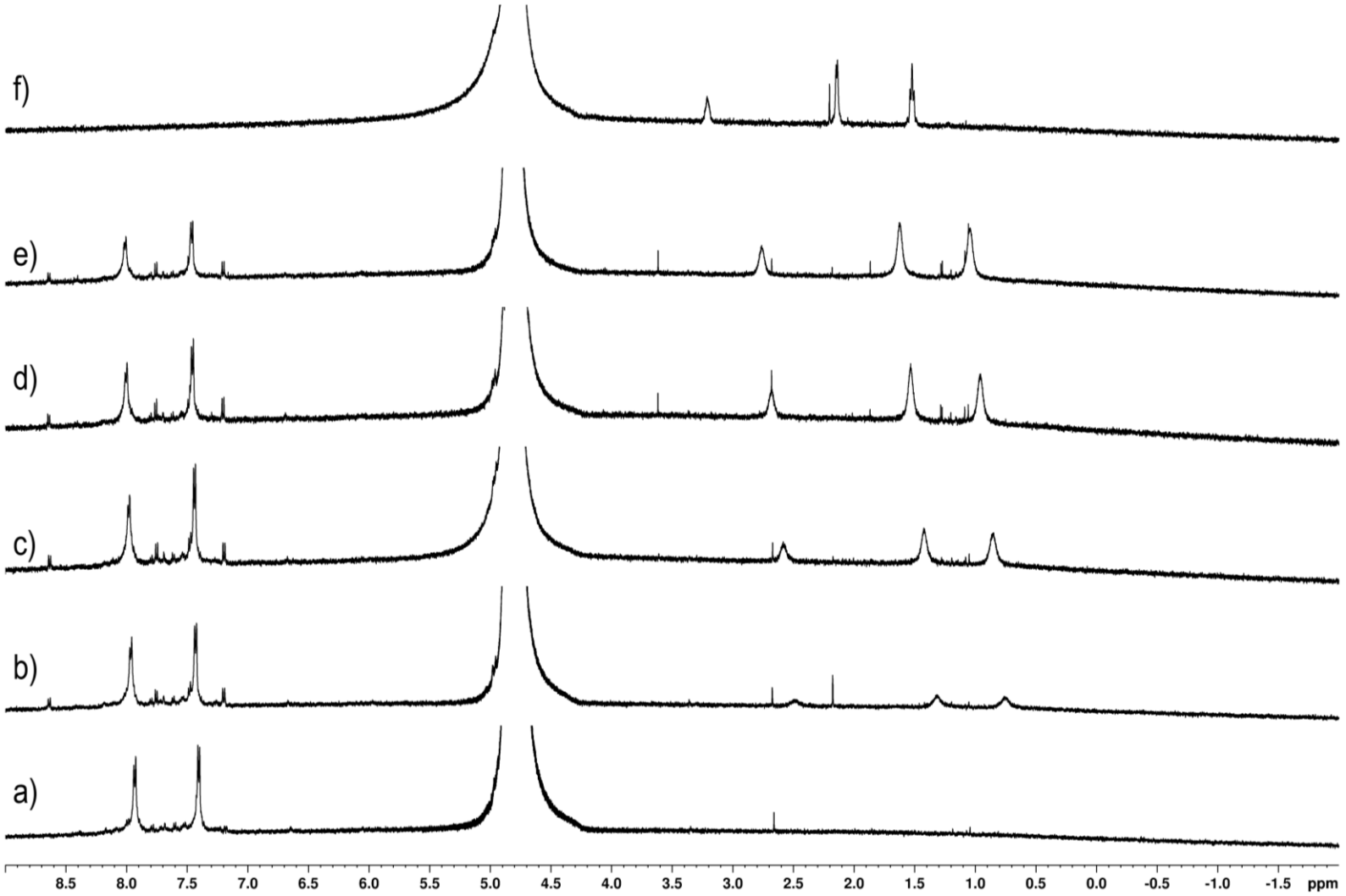


Figure S8. ^{1}H NMR spectra recorded (600 MHz, 25 °C, D_2O) for: a) Pr[6]AS (0.1 mM), b) an equimolar mixture of Pr[6]AS and **5p** (CHDA·2Cl$^-$) (0.1 mM), c) a 1:2 mixture of Pr[6]AS (0.1 mM) and **5p** (CHDA·2Cl$^-$) (0.2 mM), d) a 1:3 mixture of Pr[6]AS (0.1 mM) and **5p** (CHDA·2Cl$^-$) (0.3 mM), e) a 1:4 mixture of Pr[6]AS (0.1 mM) and **5p** (CHDA·2Cl$^-$) (0.4 mM), and f) **5p** (CHDA·2Cl$^-$) (0.4 mM).

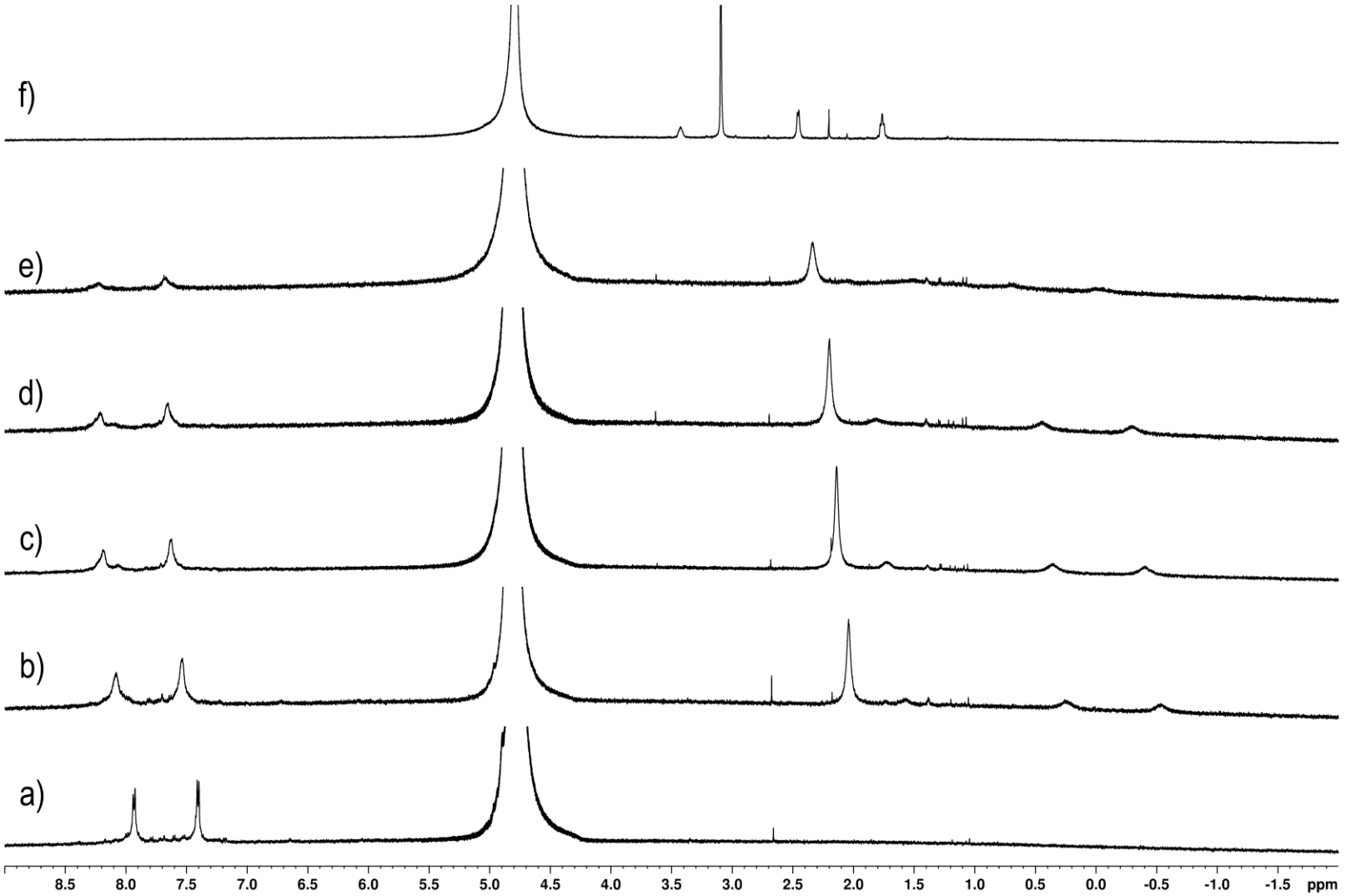


Figure S9. ^{1}H NMR spectra recorded (600 MHz, 25 °C, D_2O) for: a) Pr[6]AS (0.1 mM), b) an equimolar mixture of Pr[6]AS and **5q** (Me_6CHDA·2I$^-$) (0.1 mM), c) a 1:2 mixture of Pr[6]AS (0.1 mM) and **5q** (Me_6CHDA·2I$^-$) (0.2 mM), d) a 1:3 mixture of Pr[6]AS (0.1 mM) and **5q** (Me_6CHDA·2I$^-$) (0.3 mM), e) a 1:4 mixture of Pr[6]AS (0.1 mM) and **5q** (Me_6CHDA·2I$^-$) (0.4 mM), and f) **5q** (Me_6CHDA·2I$^-$) (0.4 mM).

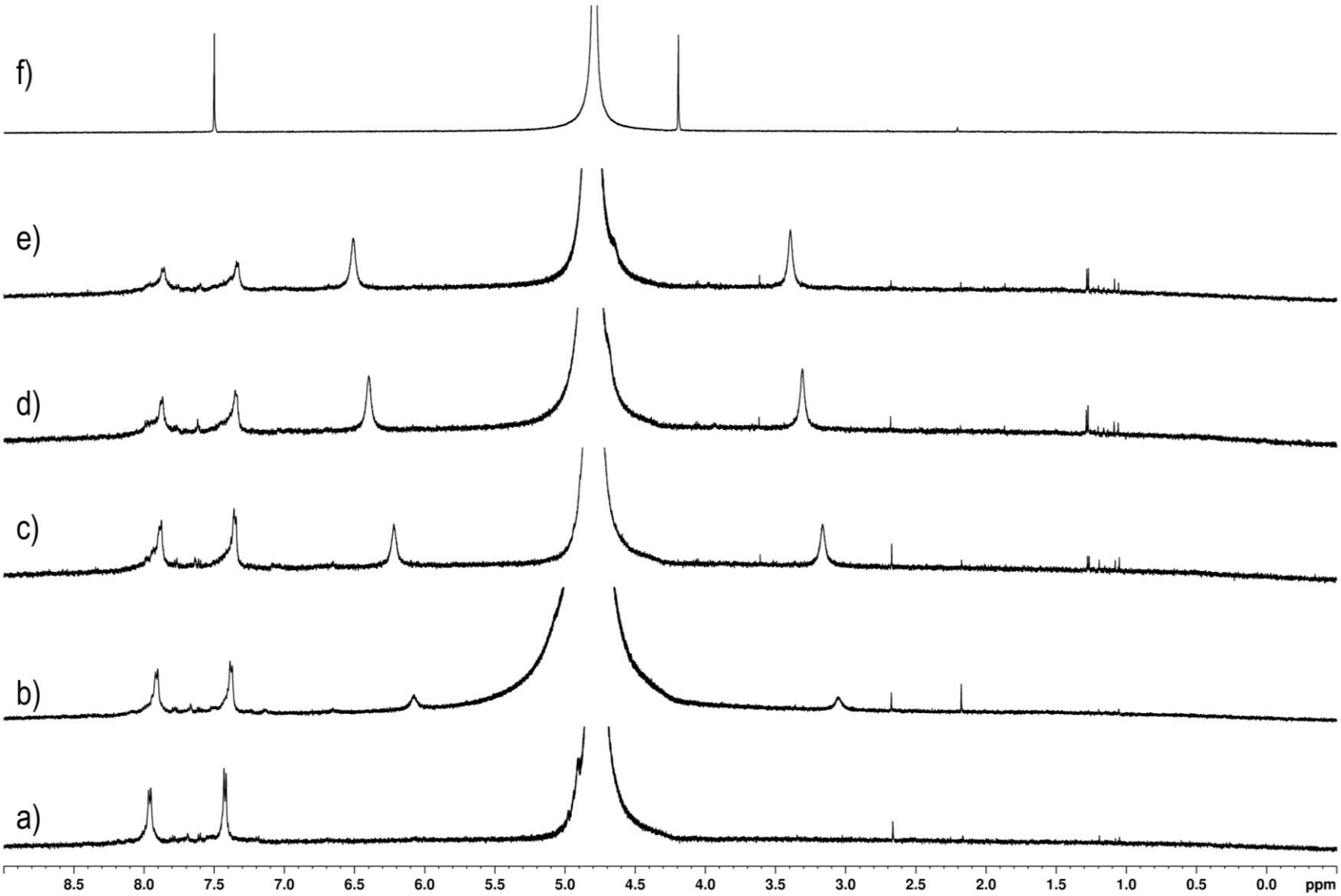


Figure S10. ^{1}H NMR spectra recorded (600 MHz, 25 ˚C, D_2O) for: a) Pr[6]AS (0.1 mM), b) an equimolar mixture of Pr[6]AS and **3p** (PXDA·2Cl^{-}) (0.1 mM), c) a 1:2 mixture of Pr[6]AS (0.1 mM) and **3p** (PXDA·2Cl^{-}) (0.2 mM), d) a 1:3 mixture of Pr[6]AS (0.1 mM) and **3p** (PXDA·2Cl^{-}) (0.3 mM), e) a 1:4 mixture of Pr[6]AS (0.1 mM) and **3p** (PXDA·2Cl^{-}) (0.4 mM), and f) **3p** (0.4 mM).

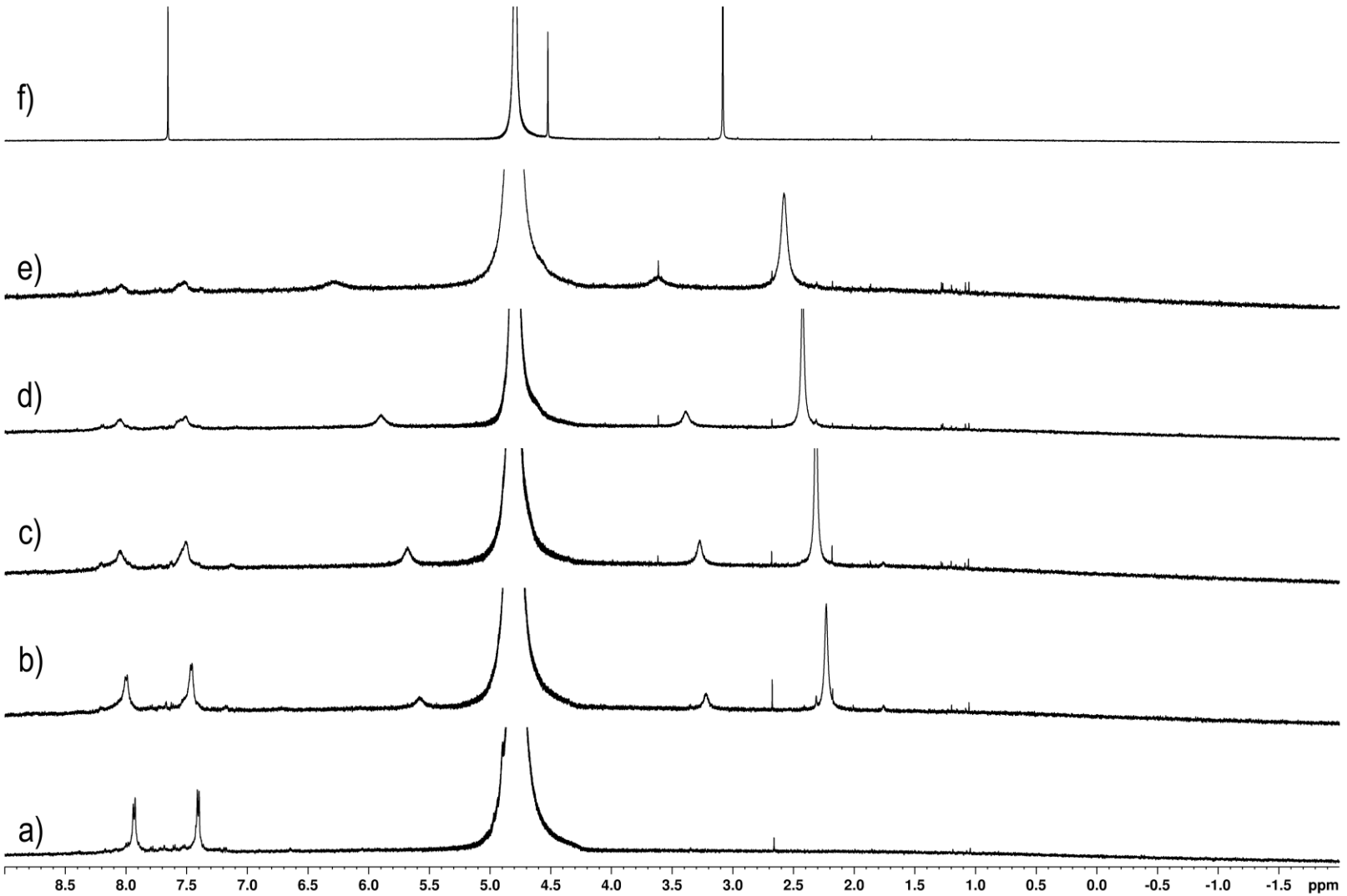


Figure S11. ^{1}H NMR spectra recorded (600 MHz, 25 °C, D_2O) for: a) Pr[6]AS (0.1 mM), b) an equimolar mixture of Pr[6]AS and **3q** (Me_6PXDA·2Br^-) (0.1 mM), c) a 1:2 mixture of Pr[6]AS (0.1 mM) and **3q** (0.2 mM), d) a 1:3 mixture of Pr[6]AS (0.1 mM) and **3q** (0.3 mM), e) a 1:4 mixture of Pr[6]AS (0.1 mM) and **3q** (0.4 mM), and f) **3q** (0.4 mM).

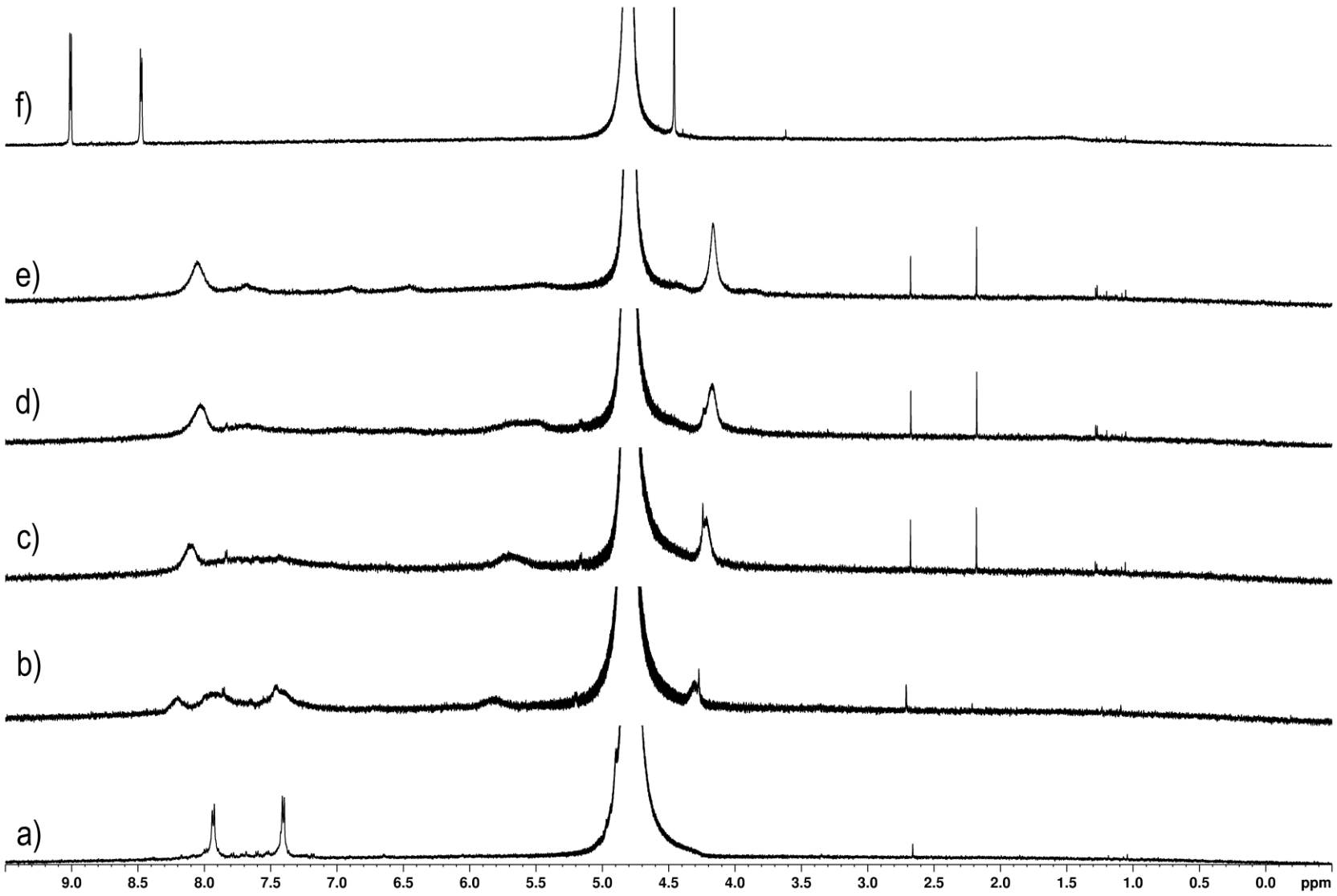


Figure S12. ^{1}H NMR spectra recorded (600 MHz, 25 °C, D_2O) for: a) Pr[6]AS (0.1 mM), b) an equimolar mixture of Pr[6]AS and **4** ($MV \cdot 2Cl^{-}$) (0.1 mM), c) a 1:2 mixture of Pr[6]AS (0.1 mM) and **4** (0.2 mM), d) a 1:3 mixture of Pr[6]AS (0.1 mM) and **4** (0.3 mM), e) a 1:4 mixture of Pr[6]AS (0.1 mM) and **4** (0.4 mM), and f) **4** (0.4 mM).

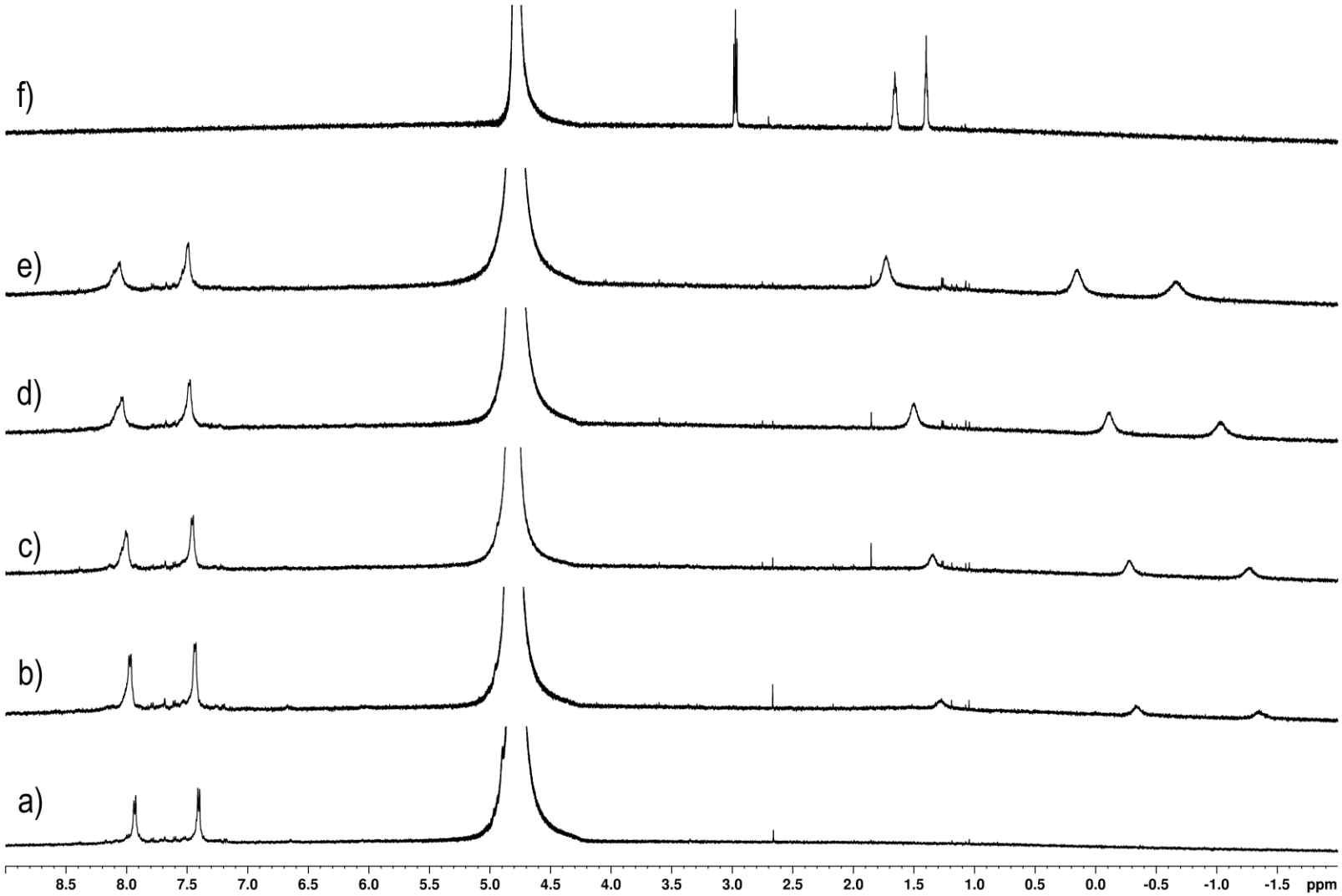


Figure S13. ^{1}H NMR spectra recorded (600 MHz, 25 °C, D_2O) for: a) Pr[6]AS (0.1 mM), b) an equimolar mixture of Pr[6]AS and **2p** (C6DA·2Cl^{-}) (0.1 mM), c) a 1:2 mixture of Pr[6]AS (0.1 mM) and **2p** (0.2 mM), d) a 1:3 mixture of Pr[6]AS (0.1 mM) and **2p** (0.3 mM), e) a 1:4 mixture of Pr[6]AS (0.1 mM) and **2p** (0.4 mM), and f) **2p** (0.4 mM).

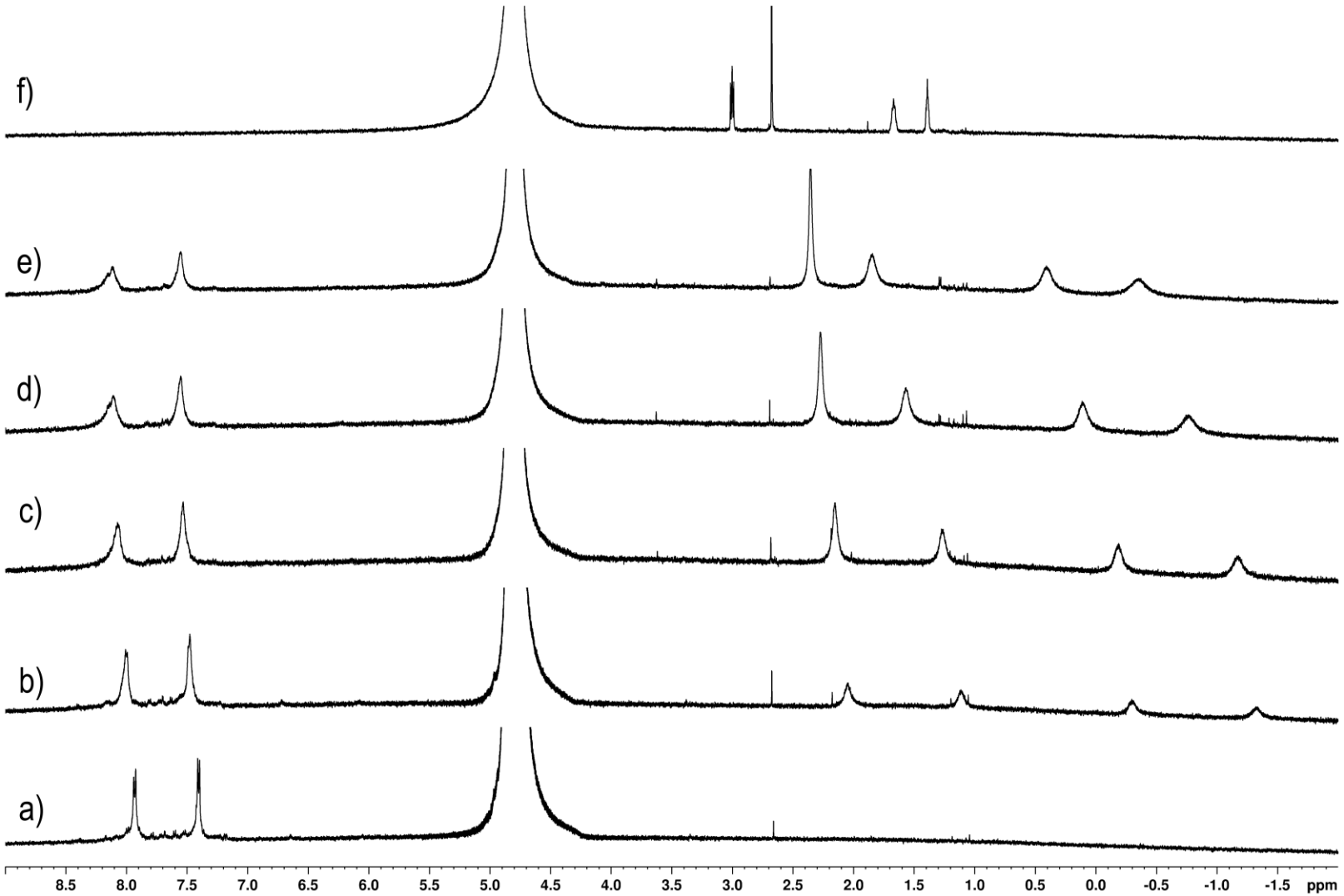


Figure S14. ^{1}H NMR spectra recorded (600 MHz, 25 °C, D_2O) for: a) Pr[6]AS (0.1 mM), b) an equimolar mixture of Pr[6]AS and **2s** (Me_2C6DA·2Cl^-) (0.1 mM), c) a 1:2 mixture of Pr[6]AS (0.1 mM) and **2s** (0.2 mM), d) a 1:3 mixture of Pr[6]AS (0.1 mM) and **2s** (0.3 mM), e) a 1:4 mixture of Pr[6]AS (0.1 mM) and **2s** (0.4 mM), and f) **2s** (0.4 mM).

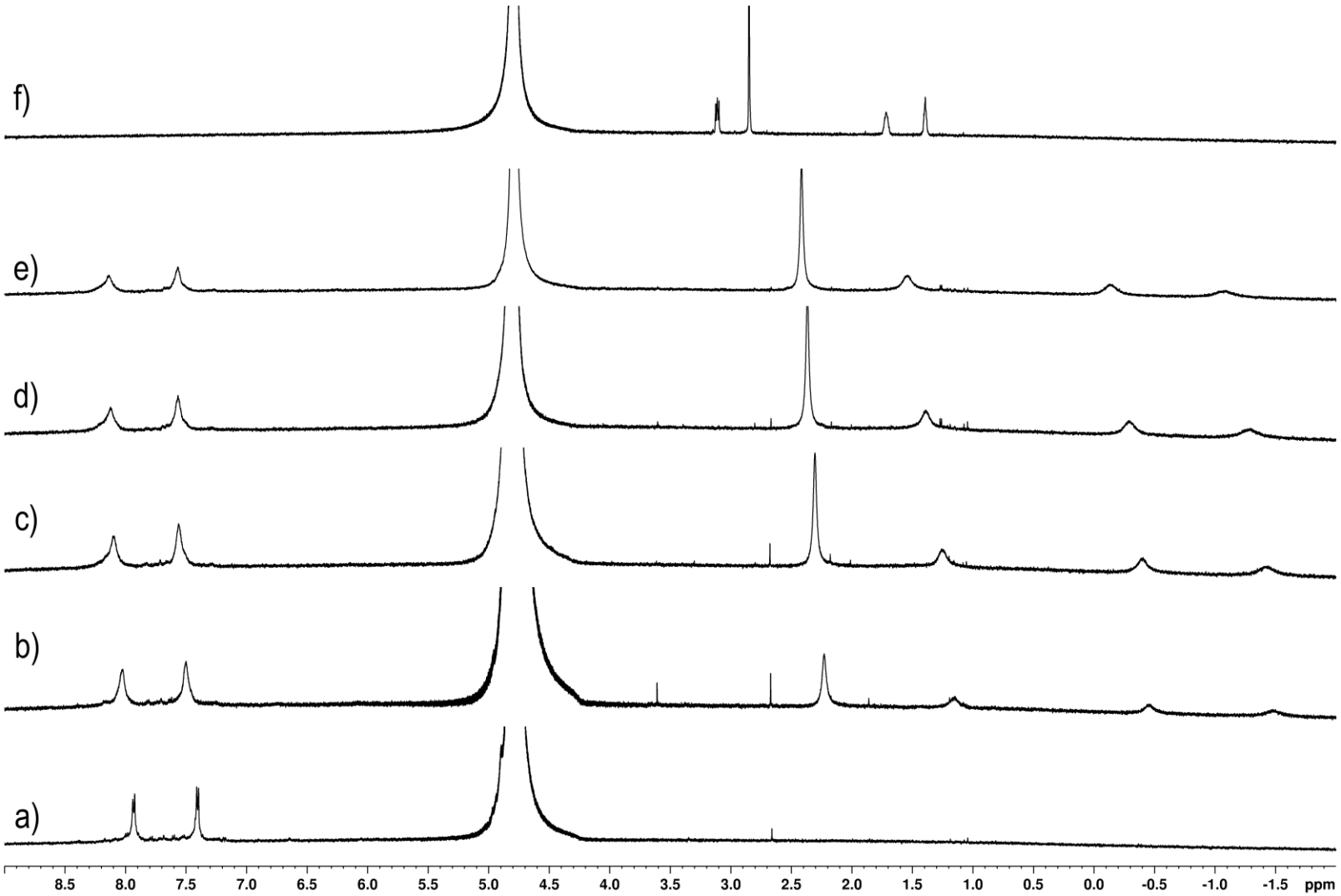


Figure S15. ^{1}H NMR spectra recorded (600 MHz, 25 °C, D_2O) for: a) Pr[6]AS (0.1 mM), b) an equimolar mixture of Pr[6]AS and **2t** ($Me_4C6DA{\cdot}2Cl^{-}$) (0.1 mM), c) a 1:2 mixture of Pr[6]AS (0.1 mM) and **2t** (0.2 mM), d) a 1:3 mixture of Pr[6]AS (0.1 mM) and **2t** (0.3 mM), e) a 1:4 mixture of Pr[6]AS (0.1 mM) and **2t** (0.4 mM), and f) **2t** (0.4 mM).

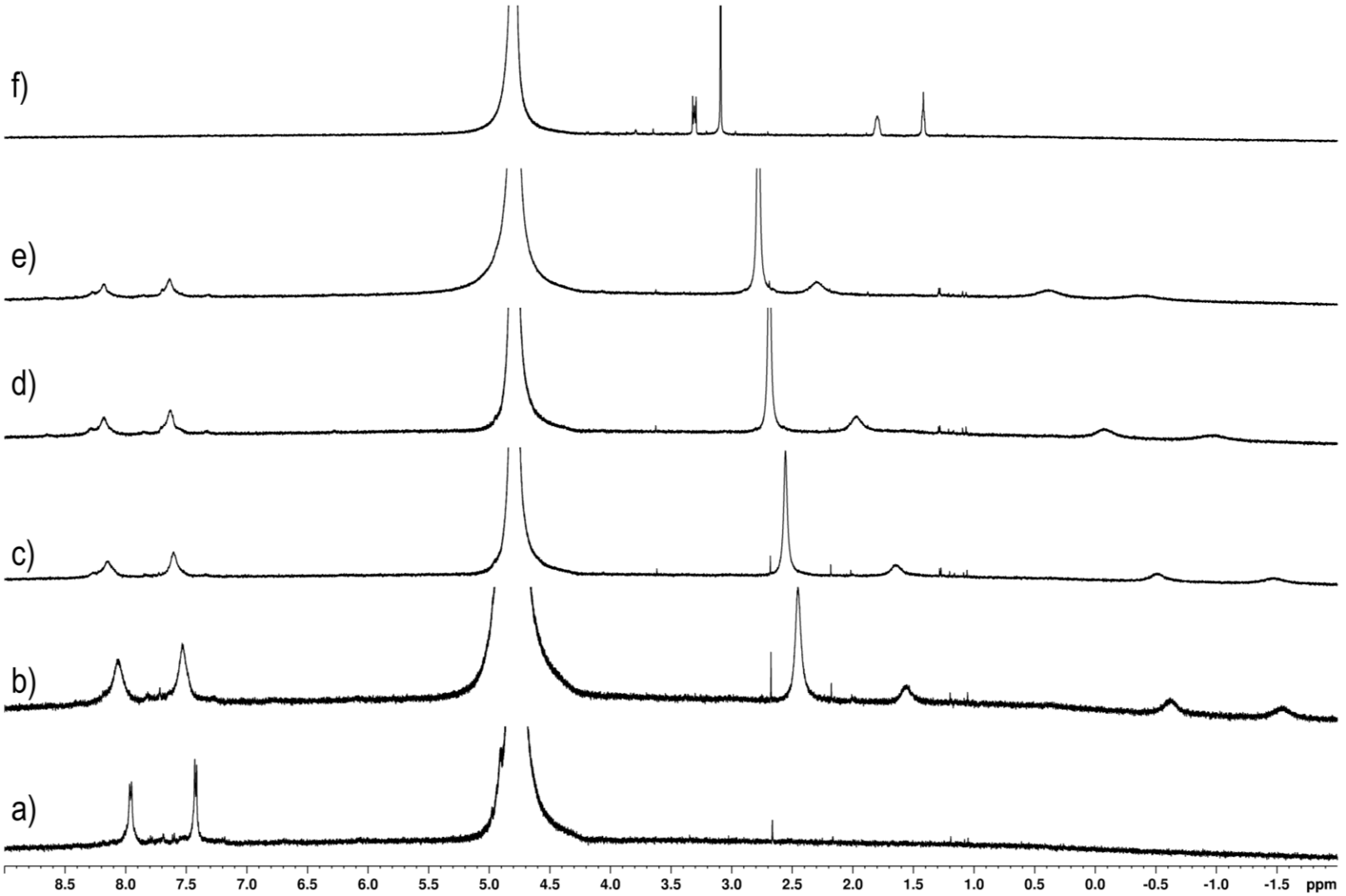


Figure S16. ^{1}H NMR spectra recorded (600 MHz, 25 °C, D_2O) for: a) Pr[6]AS (0.1 mM), b) an equimolar mixture of Pr[6]AS and **2q** (Me_6C6DA·2Br^-) (0.1 mM), c) a 1:2 mixture of Pr[6]AS (0.1 mM) and **2q** (0.2 mM), d) a 1:3 mixture of Pr[6]AS (0.1 mM) and **2q** (0.3 mM), e) a 1:4 mixture of Pr[6]AS (0.1 mM) and **2q** (0.4 mM), and f) **2q** (0.4 mM).

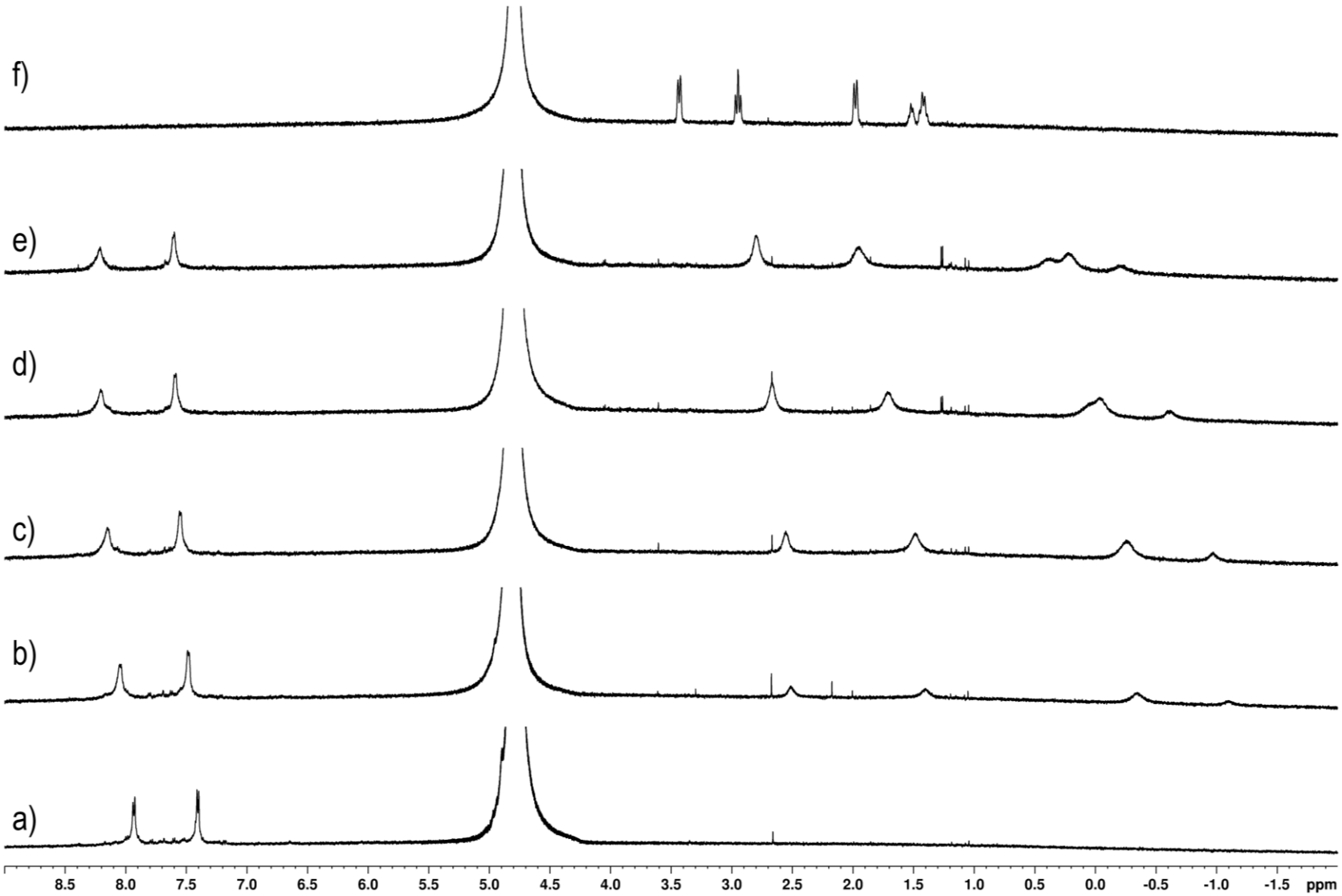


Figure S17. ^{1}H NMR spectra recorded (600 MHz, 25 °C, D_2O) for: a) Pr[6]AS (0.1 mM), b) an equimolar mixture of Pr[6]AS and **6s** (Bipip·2Cl^{-}) (0.1 mM), c) a 1:2 mixture of Pr[6]AS (0.1 mM) and **6s** (0.2 mM), d) a 1:3 mixture of Pr[6]AS (0.1 mM) and **6s** (0.3 mM), e) a 1:4 mixture of Pr[6]AS (0.1 mM) and **6s** (0.4 mM), and f) **6s** (0.4 mM).

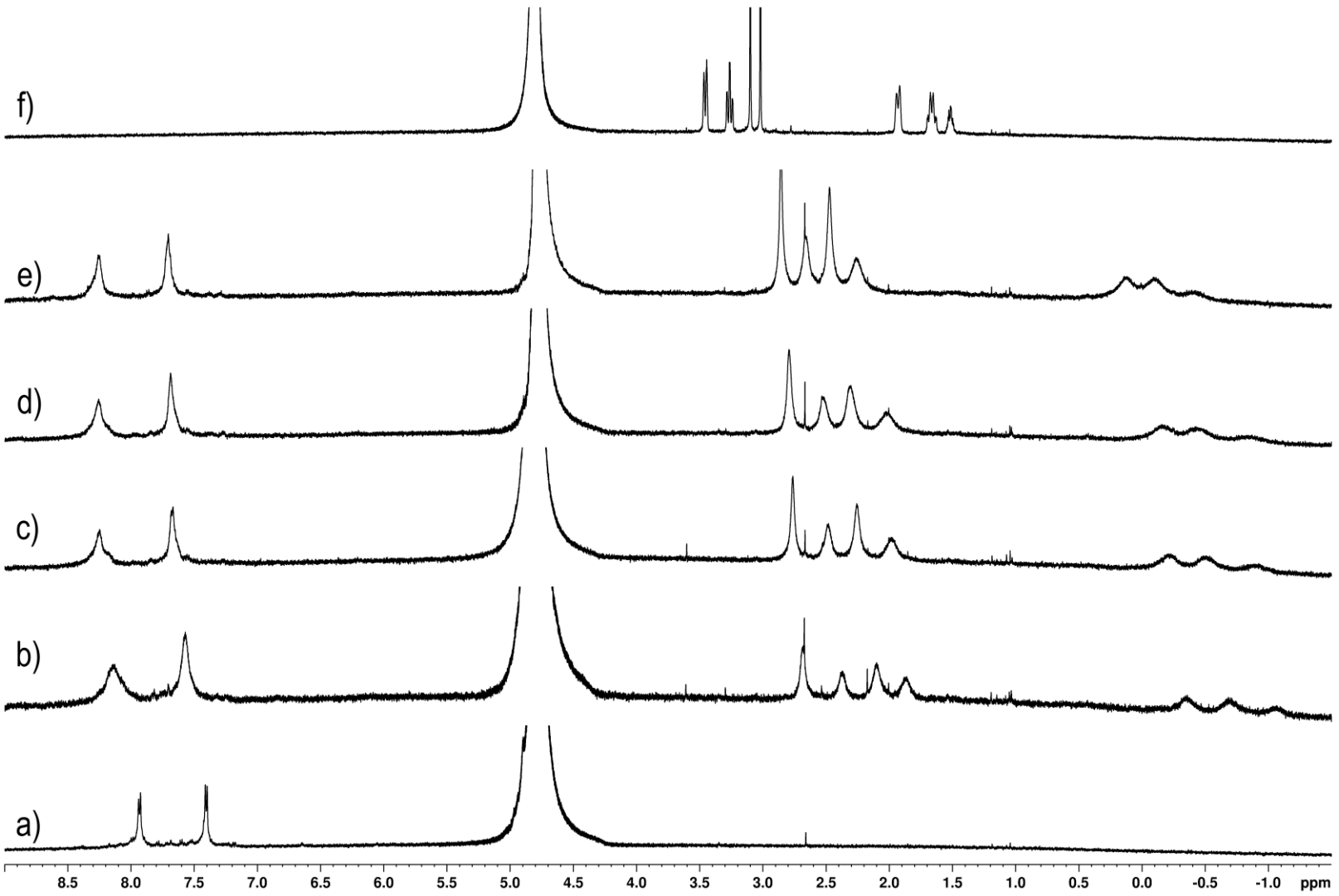


Figure S18. ^{1}H NMR spectra recorded (600 MHz, 25 °C, D_2O) for: a) Pr[6]AS (0.1 mM), b) an equimolar mixture of Pr[6]AS and **6q** (Me_4Bipip·2I^-) (0.1 mM), c) a 1:2 mixture of Pr[6]AS (0.1 mM) and **6q** (0.2 mM), d) a 1:3 mixture of Pr[6]AS (0.1 mM) and **6q** (0.3 mM), e) a 1:4 mixture of Pr[6]AS (0.1 mM) and **6q** (0.4 mM), and f) **6q** (0.4 mM).

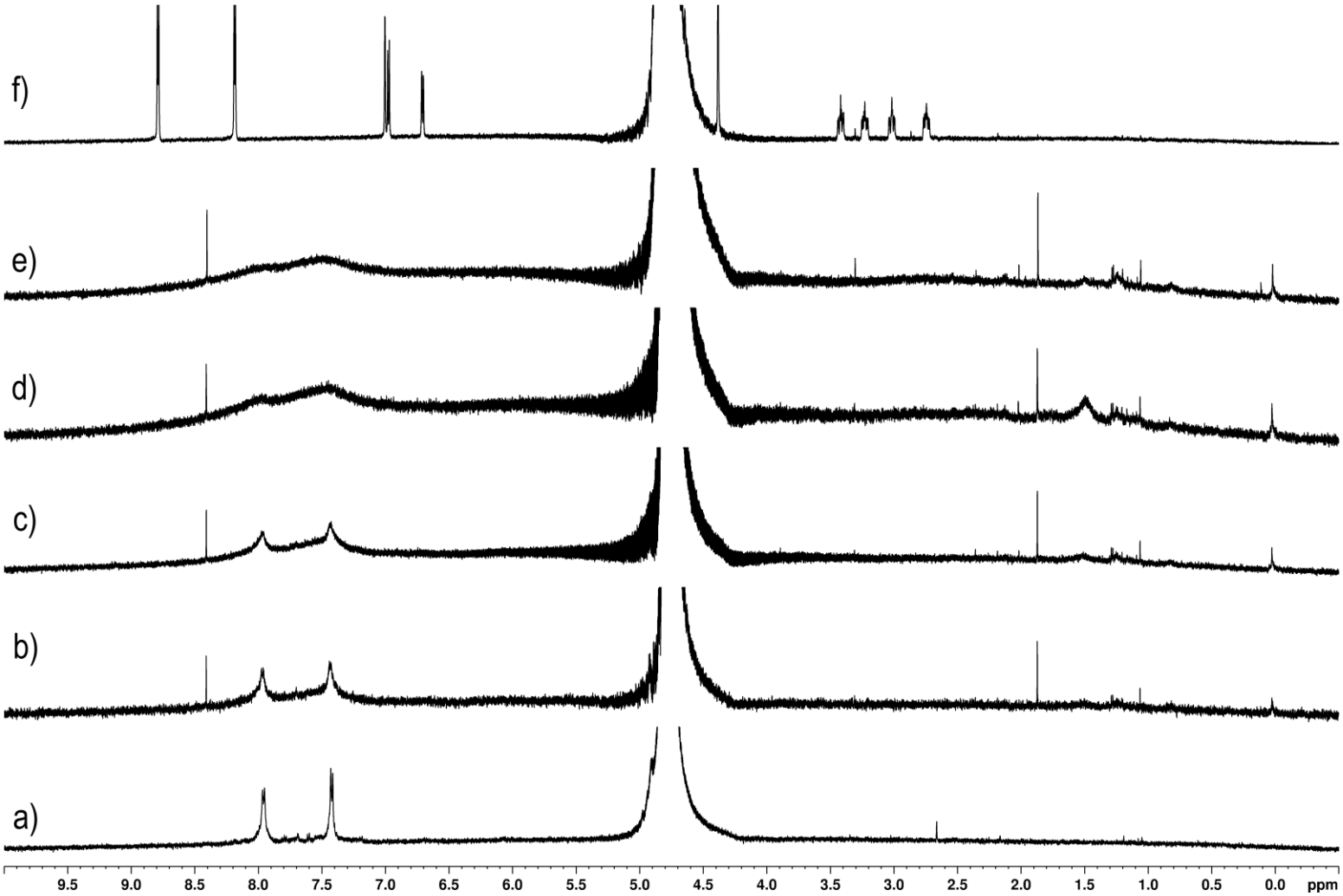


Figure S19. ^{1}H NMR spectra recorded (600 MHz, 25 °C, D_2O) for: a) Pr[6]AS (0.1 mM), b) an equimolar mixture of Pr[6]AS and **7** (PPCP·2I$^-$) (0.1 mM), c) a 1:2 mixture of Pr[6]AS (0.1 mM) and **7** (0.2 mM), d) a 1:3 mixture of Pr[6]AS (0.1 mM) and **7** (0.3 mM), e) a 1:4 mixture of Pr[6]AS (0.1 mM) and **7** (0.4 mM), and f) **7** (0.4 mM).

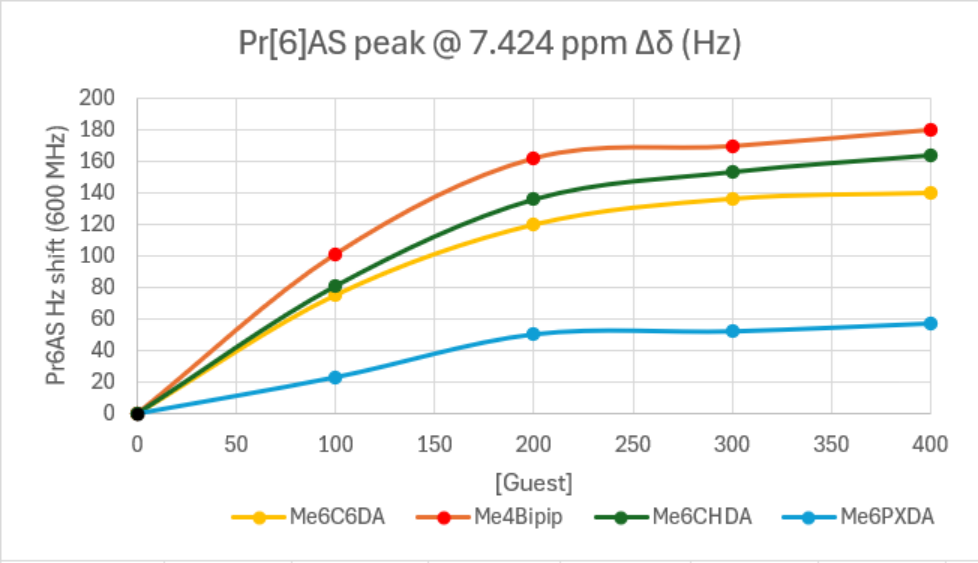


Figure S20. Plot of the change in chemical shift (Hz) observed for H_b of Pr[6]AS (100 μM) upon titration with guest (100, 200, 300, 400 μM). Color code: **2q**, yellow; **6q**, red; **5q**, green; **3q**, blue.

Isothermal titration calorimetry (ITC) experiments. All ITC experiments were conducted in the 200 μL working volume of the sample cell of the PEAQ ITC instrument. In each case, the host and guest solutions were prepared in PBS buffer (pH 7.4) prepared using Tablets (Catalog number 2810305) from MP Biomedicals. We used an injection syringe of 50 μL capacity. The sample cell was rinsed (using the PEAQ ITC integrated washing protocol), washed with 100 μL of HPLC-grade H_2O (manually injected using the syringe) 3 times to ensure that any remnants of cleaning solvent from the machine was removed, and then coated with 200 μL of cell solution, which was then discarded, prior to each usage. The sample cell was then filled to capacity (200 μL) with the host solution using the following process to minimize the potential for air bubbles to form: insert the syringe into sample cell, with about 1–2 mm of space between the syringe tip and the bottom of the cell, and slowly inject the cell solution into the cavity until the solution is just barely visible in the bowl above the sample cell. Proceed to vigorously pull up and re-inject the host solution (about 20–50 μL worth) several times in order to agitate the solution and push out any air pockets present in the sample cell. If any air is present within the cell, then small bubbles should come to the surface of the bowl during each agitation. After the agitation process is complete (no bubble should rise), pull up about 50 μL of host solution and re-inject it as the syringe is slowly pulled out of the cell. Pull out any remaining host solution present in the bowl and discard. The guest solution was then titrated in by the instrument in equal increments of time (first injection = 0.4 μL with subsequent 18 injections = 2 μL). The binding data was fitted using the sequential binding model in MicroCal PEAQ-ITC analysis software.

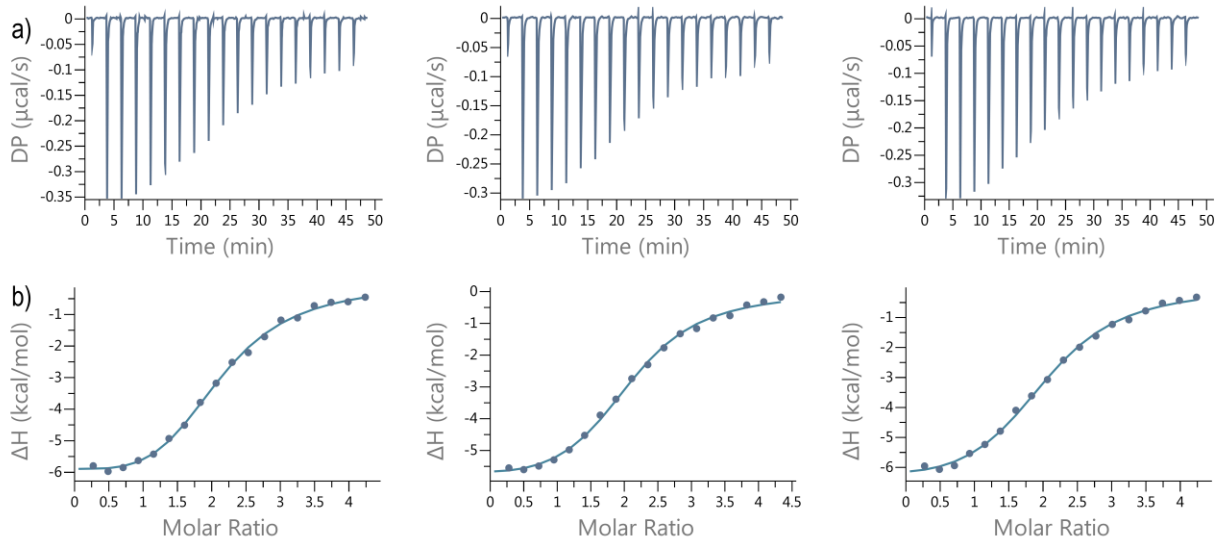


Figure S21. a) Plots of DP vs. time from the direct titration of molecular container Pr[6]AS (10 µM) with **5q** (Me_6CHDA·2I^-) (200 µM) in PBS (pH 7.4); b) plots of Δ*H* as a function of guest:host molar ratio. The solid lines represent the best non-linear fit of the data to a sequential binding model (triplicate averages for Pr[6]AS·**5q**: K_{a1} = (1.41 ± 0.03) × 10^6 M^{-1}, ΔH_1 = −6.36 ± 0.05 kcal/mol, $-T\Delta S_1$ = −2.03 ± 0.06 kcal/mol; K_{a2} = (2.55 ± 0.04) × 10^5 M^{-1}, ΔH_2 = −7.56 ± 0.22 kcal/mol, $-T\Delta S_2$ = 0.18 ± 0.22 kcal/mol; $K_{a1}\cdot K_{a2}$ = (3.62 ± 0.08) × 10^{11} M^{-2}, ΔH = −13.92 ± 0.23 kcal/mol, $-T\Delta S$ = −1.85 ± 0.23 kcal/mol).

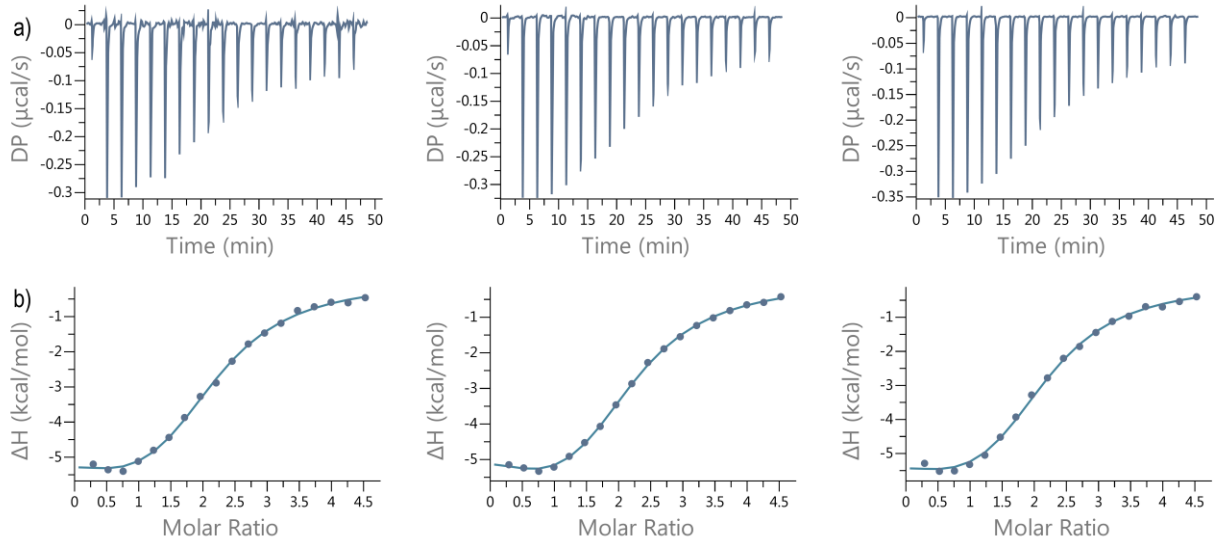


Figure S22. a) Plots of DP vs. time from the direct titration of molecular container **Pr[6]AS** (10 µM) with **3q** (**Me_6PXDA**•2Br^-) (200 µM) in PBS (pH 7.4); b) plots of Δ*H* as a function of guest:host molar ratio. The solid lines represent the best non-linear fit of the data to a sequential binding model (triplicate averages for **Pr[6]AS·3q**: K_{a1} = (2.23 ± 0.14) × 10^6 M^{-1}, ΔH_1 = −5.82 ± 0.31 kcal/mol, $-T\Delta S_1$ = −2.84 ± 0.31 kcal/mol; K_{a2} = (2.31 ± 0.19) × 10^5 M^{-1}, ΔH_2 = −7.87 ± 0.20 kcal/mol, $-T\Delta S_2$ = 0.55 ± 0.20 kcal/mol; $K_{a1}\cdot K_{a2}$ = (5.14 ± 0.53) × 10^{10} M^{-2}, ΔH = −13.69 ± 0.37 kcal/mol, $-T\Delta S$ = −2.29 ± 0.37 kcal/mol).

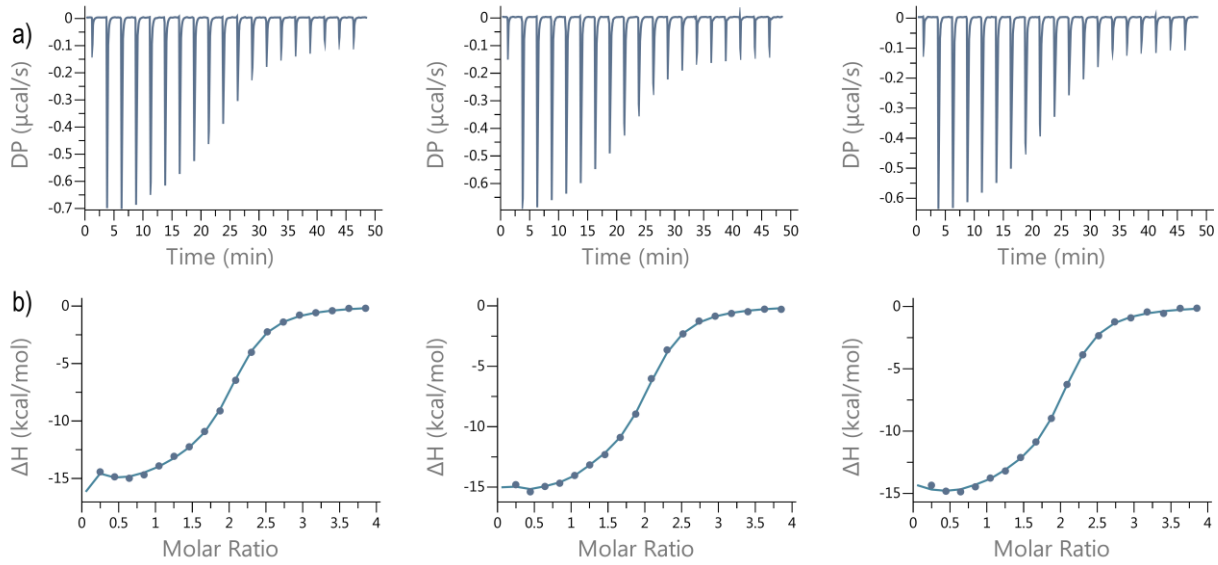


Figure S23. a) Plots of DP vs. time from the competitive titration of molecular container Pr[6]AS (10 µM) with **4** (MV·2Cl$^-$) (200 µM) in PBS (pH 7.4); b) plots of Δ*H* as a function of guest:host molar ratio. The solid lines represent the best non-linear fit of the data to a sequential binding model (triplicate averages for Pr[6]AS·**4**: K_{a1} = (4.48 ± 0.04) × 10^7 M^{-1}, ΔH_1 = −15.07 ± 0.08 kcal/mol, $-T\Delta S_1$ = 4.63 ± 0.08 kcal/mol; K_{a2} = (1.55 ± 0.02) × 10^6 M^{-1}, ΔH_2 = −13.77 ± 0.09 kcal/mol, $-T\Delta S_2$ = 5.32 ± 0.09 kcal/mol; $K_{a1}\cdot K_{a2}$ = (6.94 ± 0.12) × 10^{13} M^{-2}, ΔH = −28.80 ± 0.12 kcal/mol, $-T\Delta S$ = 9.95 ± 0.10 kcal/mol).

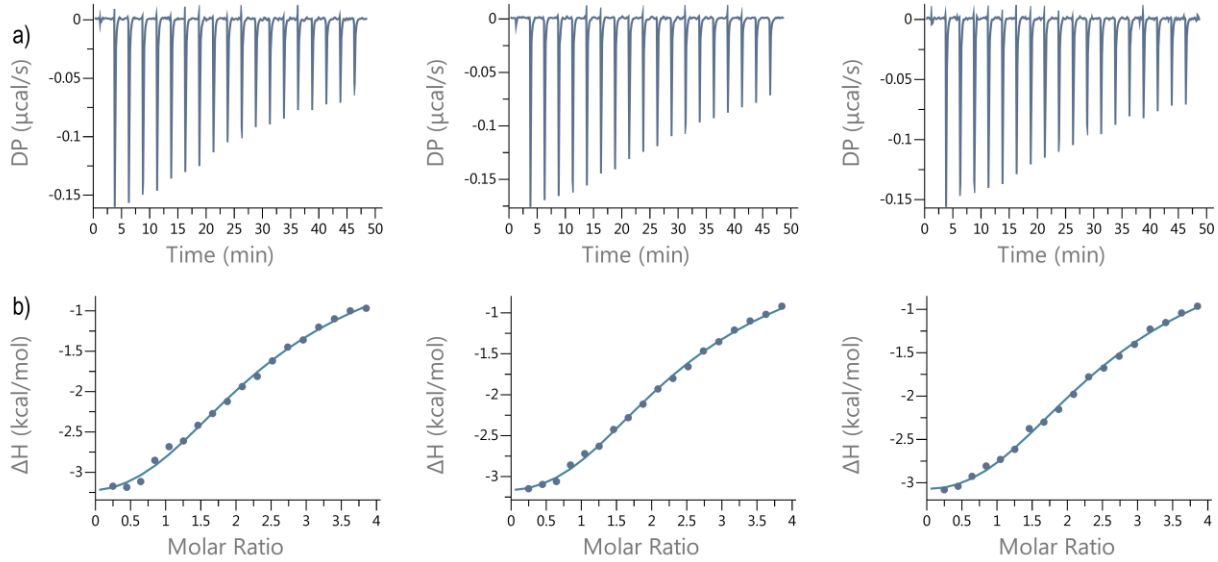


Figure S24. a) Plots of DP vs. time from the competitive titration of molecular container Pr[6]AS (10 µM) with **2p** (C6DA·2Cl$^-$) (200 µM) in PBS (pH 7.4) from the syringe; b) plots of Δ*H* as a function of guest:host molar ratio. The solid lines represent the best non-linear fit of the data to a sequential binding model (triplicate averages for Pr[6]AS·**2p**: K_{a1} = (3.58 ± 0.55) × 10^5 M^{-1}, ΔH_1 = −4.05 ± 0.83 kcal/mol, $-T\Delta S_1$ = −3.52 ± 0.83 kcal/mol; K_{a2} = (4.00 ± 1.17) × 10^4 M^{-1}, ΔH_2 = −9.62 ± 1.80 kcal/mol, $-T\Delta S_2$ = 3.34 ± 1.81 kcal/mol; $K_{a1}\cdot K_{a2}$ = (1.43 ± 0.47) × 10^{10} M^{-2}, ΔH = −13.67 ± 1.98 kcal/mol, $-T\Delta S$ = −0.18 ± 1.98 kcal/mol).

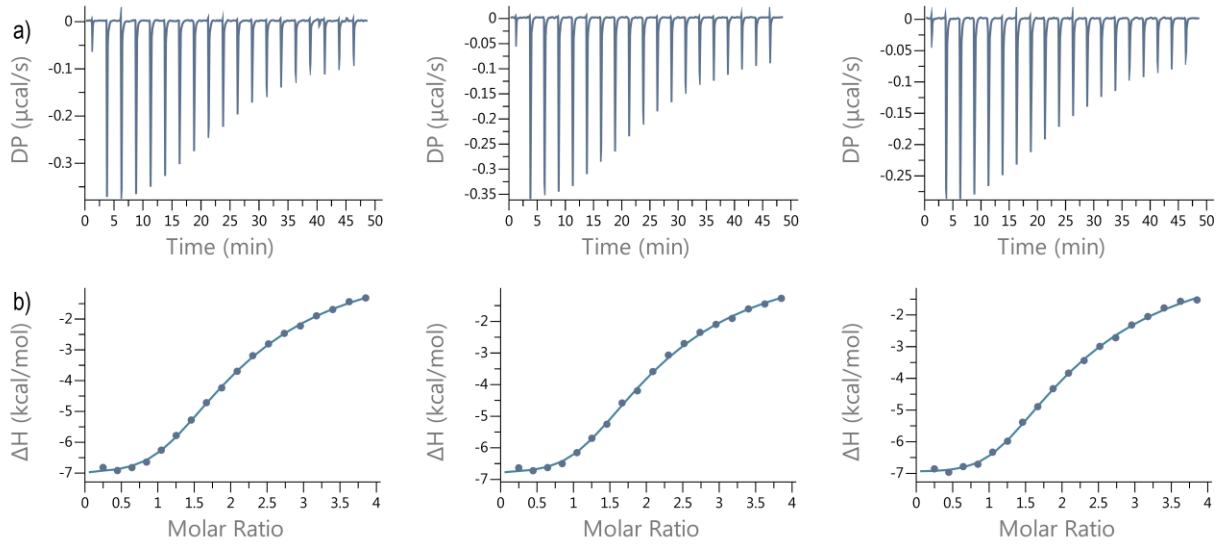


Figure S25. a) Plots of DP vs. time from the competitive titration of molecular container Pr[6]AS (10 µM) with **2s** (Me_2C6DA·2Cl^-) (200 µM) in PBS (pH 7.4) from the syringe; b) plots of Δ*H* as a function of guest:host molar ratio. The solid lines represent the best non-linear fit of the data to a sequential binding model (triplicate averages for Pr[6]AS·**2s**: K_{a1} = (1.59 ± 0.02) × 10^6 M^{-1}, ΔH_1 = −7.35 ± 0.09 kcal/mol, $-T\Delta S_1$ = −1.11 ± 0.09 kcal/mol; K_{a2} = (8.27 ± 0.23) × 10^4 M^{-1}, ΔH_2 = −14.23 ± 0.33 kcal/mol, $-T\Delta S_2$ = 7.52 ± 0.33 kcal/mol; $K_{a1}\cdot K_{a2}$ = (1.31 ± 0.04) × 10^{11} M^{-2}, Δ*H* = −21.58 ± 0.34 kcal/mol, $-T\Delta S$ = 6.41 ± 0.34 kcal/mol).

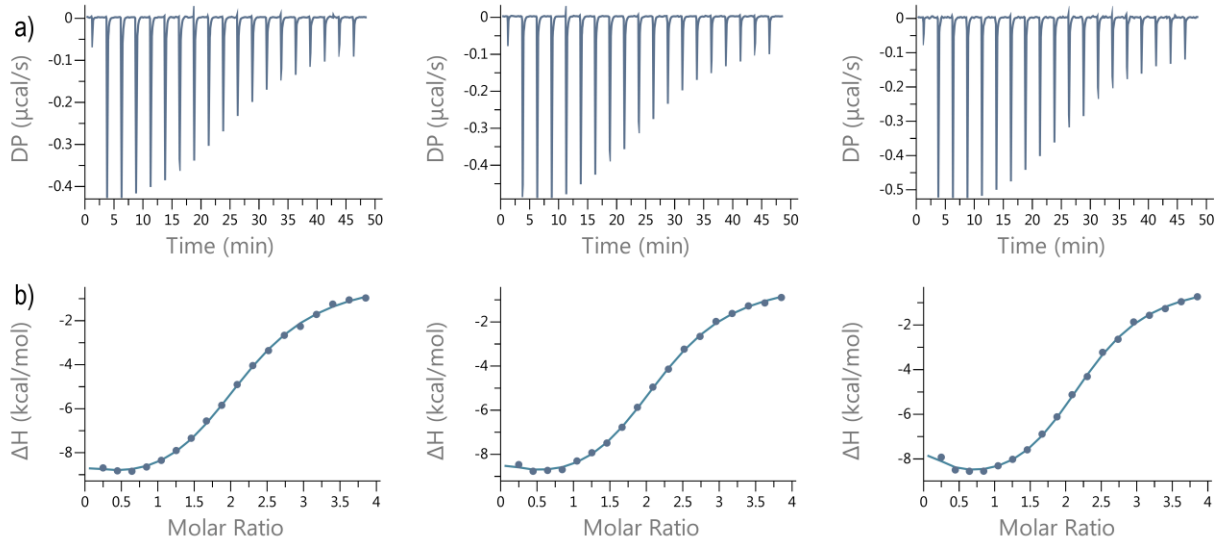


Figure S26. a) Plots of DP vs. time from the direct titration of molecular container Pr[6]AS (10 µM) with **2t** (Me_4C6DA·2Cl^-) (200 µM) in PBS (pH 7.4); b) plots of Δ*H* as a function of guest:host molar ratio. The solid lines represent the best non-linear fit of the data to a sequential binding model (triplicate averages for Pr[6]AS·**2t**: K_{a1} = (8.45 ± 1.00) × 10^5 M^{-1}, ΔH_1 = −9.35 ± 1.11 kcal/mol, $-T\Delta S_1$ = 1.27 ± 1.11 kcal/mol; K_{a2} = (3.40 ± 0.18) × 10^5 M^{-1}, ΔH_2 = −12.37 ± 1.35 kcal/mol, $-T\Delta S_2$ = 4.82 ± 1.35 kcal/mol; $K_{a1}\cdot K_{a2}$ = (2.87 ± 0.37) × 10^{11} M^{-2}, Δ*H* = −21.72 ± 1.75 kcal/mol, $-T\Delta S$ = 6.09 ± 1.49 kcal/mol).

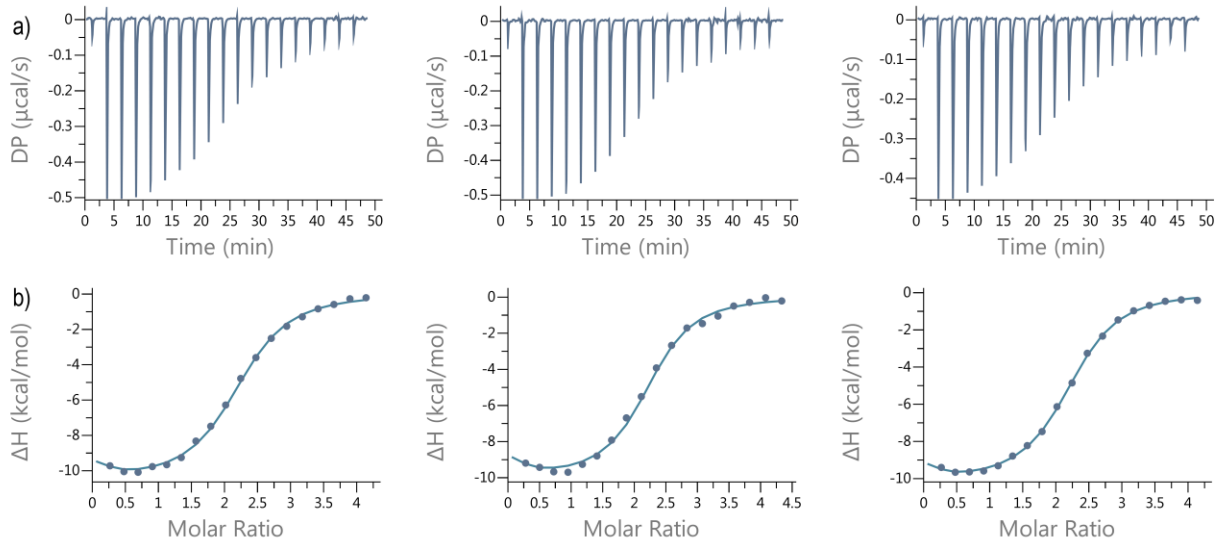


Figure S27. a) Plots of DP vs. time from the direct titration of molecular container Pr[6]AS (10 µM) with **2q** ($Me_6C6DA{\cdot}2Br^-$) (200 µM) in PBS (pH 7.4); b) plots of Δ*H* as a function of guest:host molar ratio. The solid lines represent the best non-linear fit of the data to a sequential binding model (triplicate averages for Pr[6]AS·**2q**: K_{a1} = (6.42 ± 0.37) × 10^5 M^{-1}, ΔH_1 = −10.57 ± 0.83 kcal/mol, $-T\Delta S_1$ = 2.64 ± 0.83 kcal/mol; K_{a2} = (9.49 ± 0.23) × 10^5 M^{-1}, ΔH_2 = −11.47 ± 1.04 kcal/mol, $-T\Delta S_2$ = 3.31 ± 1.04 kcal/mol; $K_{a1}{\cdot}K_{a2}$ = (6.09 ± 0.38) × 10^{11} M^{-2}, Δ*H* = −22.14 ± 1.33 kcal/mol, $-T\Delta S$ = 5.95 ± 1.33 kcal/mol).

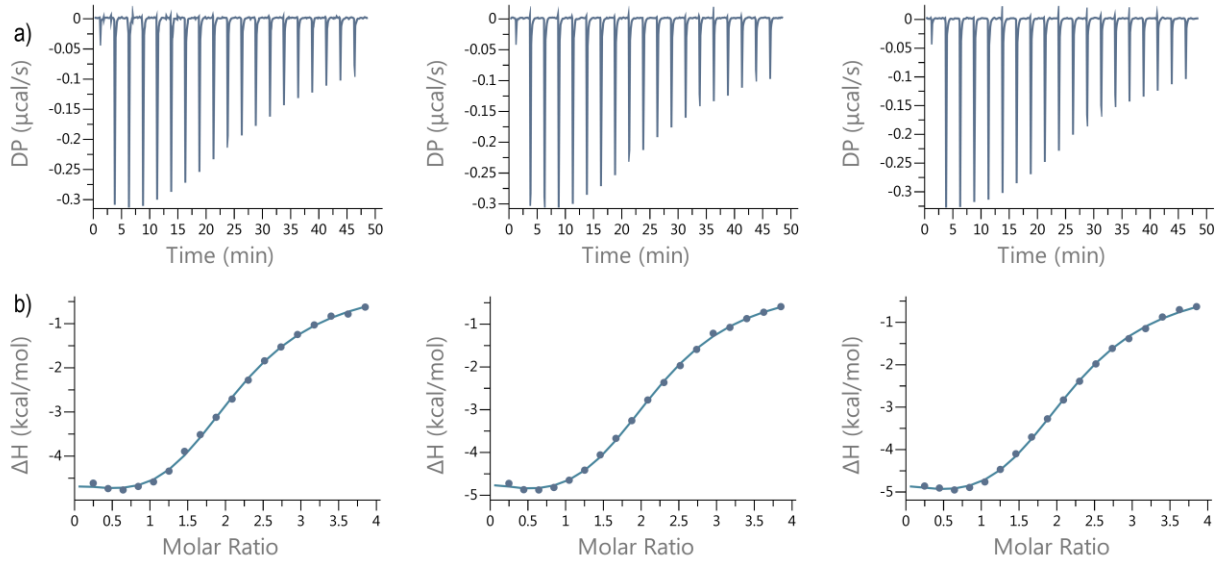


Figure S28. a) Plots of DP vs. time from the direct titration of molecular container **Pr[6]AS** (10 µM) with **6s** ($Bipip{\cdot}2Cl^-$) (200 µM) in PBS (pH 7.4); b) plots of Δ*H* as a function of guest:host molar ratio. The solid lines represent the best non-linear fit of the data to a sequential binding model (triplicate averages for Pr[6]AS·**6s**: K_{a1} = (1.11 ± 0.01) × 10^6 M^{-1}, ΔH_1 = −5.23 ± 0.02 kcal/mol, $-T\Delta S_1$ = −3.01 ± 0.02 kcal/mol; K_{a2} = (2.09 ± 0.02) × 10^5 M^{-1}, ΔH_2 = −7.64 ± 0.14 kcal/mol, $-T\Delta S_2$ = 0.39 ± 0.14 kcal/mol; $K_{a1}{\cdot}K_{a2}$ = (2.31 ± 0.03) × 10^{11} M^{-2}, Δ*H* = −12.87 ± 0.14 kcal/mol, $-T\Delta S$ = −2.62 ± 0.14 kcal/mol).

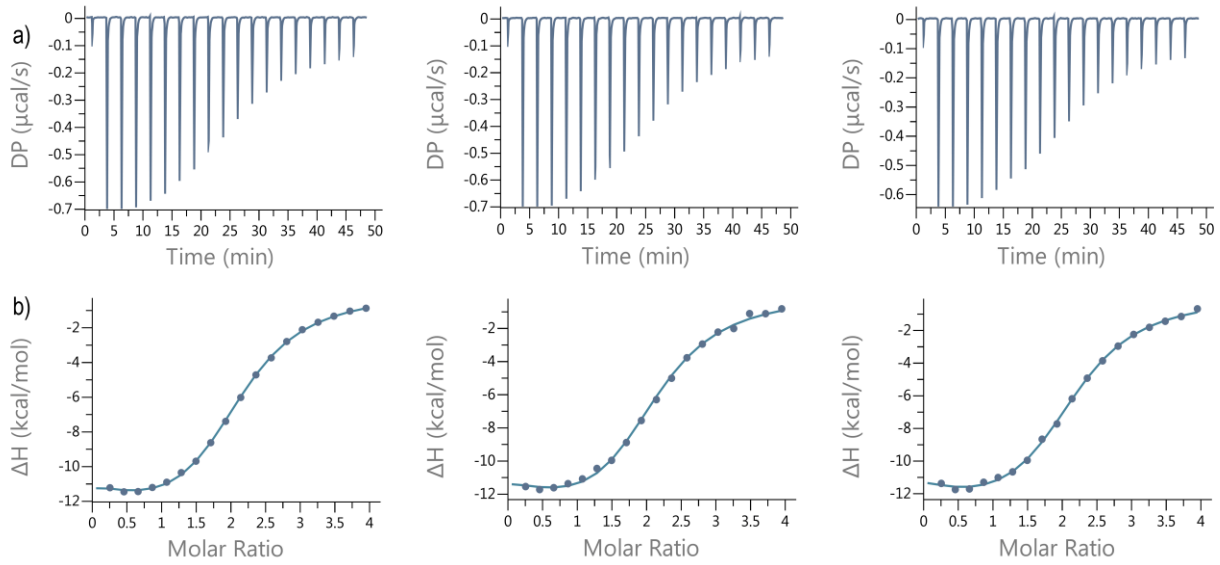


Figure S29. a) Plots of DP vs. time from the direct titration of molecular container Pr[6]AS (10 µM) with **6q** ($Me_4Bipip{\cdot}2I^-$) (200 µM) in PBS buffer (pH 7.4); b) plots of the ΔH as a function of guest:host molar ratio. The solid lines represent the best non-linear fit of the data to a sequential binding model (triplicate averages for Pr[6]AS·**6q**: K_{a1} = (1.28 ± 0.11) × 10^6 M^{-1}, ΔH_1 = −12.33 ± 1.15 kcal/mol, $-T\Delta S_1$ = 4.00 ± 1.15 kcal/mol; K_{a2} = (6.48 ± 0.31) × 10^5 M^{-1}, ΔH_2 = −12.63 ± 1.42 kcal/mol, $-T\Delta S_2$ = 4.70 ± 1.42 kcal/mol; $K_{a1}{\cdot}K_{a2}$ = (8.29 ± 0.82) × 10^{11} M^{-2}, ΔH = −24.96 ± 1.83 kcal/mol, $-T\Delta S$ = 8.70 ± 1.83 kcal/mol).

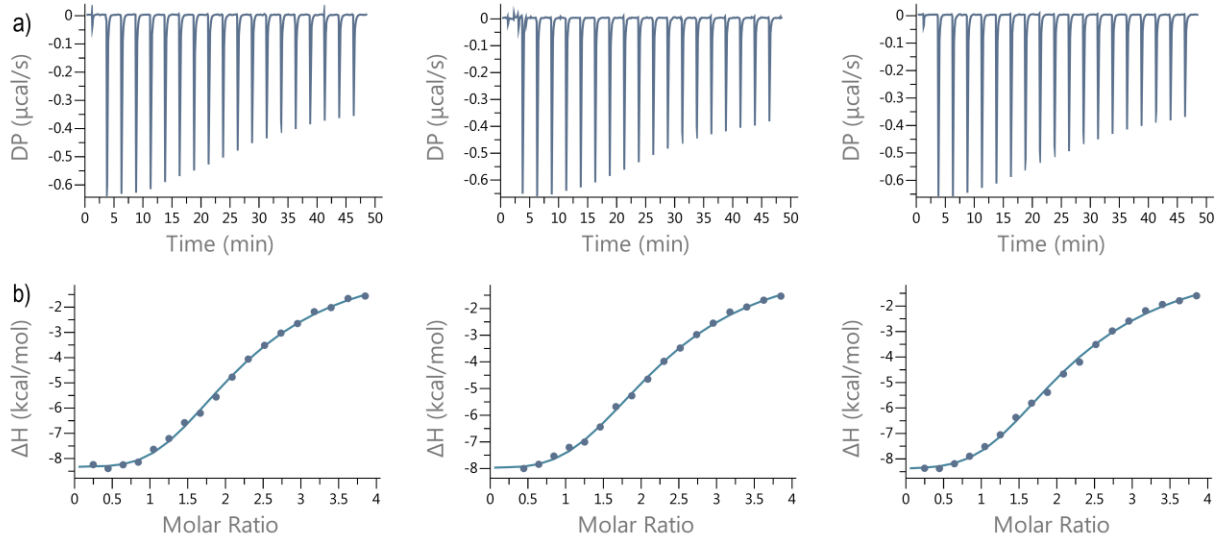


Figure S30. a) Plots of DP vs. time from the direct titration of molecular container Pr[6]AS (10 µM) with **7** ($PPCP{\cdot}2I^-$) (200 µM) in PBS buffer (pH 7.4); b) plots of the ΔH as a function of guest:host molar ratio. The solid lines represent the best non-linear fit of the data to a sequential binding model (triplicate averages for Pr[6]AS·**7**: K_{a1} = (1.02 ± 0.08) × 10^6 M^{-1}, ΔH_1 = −9.08 ± 0.82 kcal/mol, $-T\Delta S_1$ = 0.88 ± 0.82 kcal/mol; K_{a2} = (1.04 ± 0.13) × 10^5 M^{-1}, ΔH_2 = −15.77 ± 0.69 kcal/mol, $-T\Delta S_2$ = 8.92 ± 0.69 kcal/mol; $K_{a1}{\cdot}K_{a2}$ = (1.06 ± 0.16) × 10^{11} M^{-2}, ΔH = −24.85 ± 1.07 kcal/mol, $-T\Delta S$ = 9.80 ± 1.07 kcal/mol).

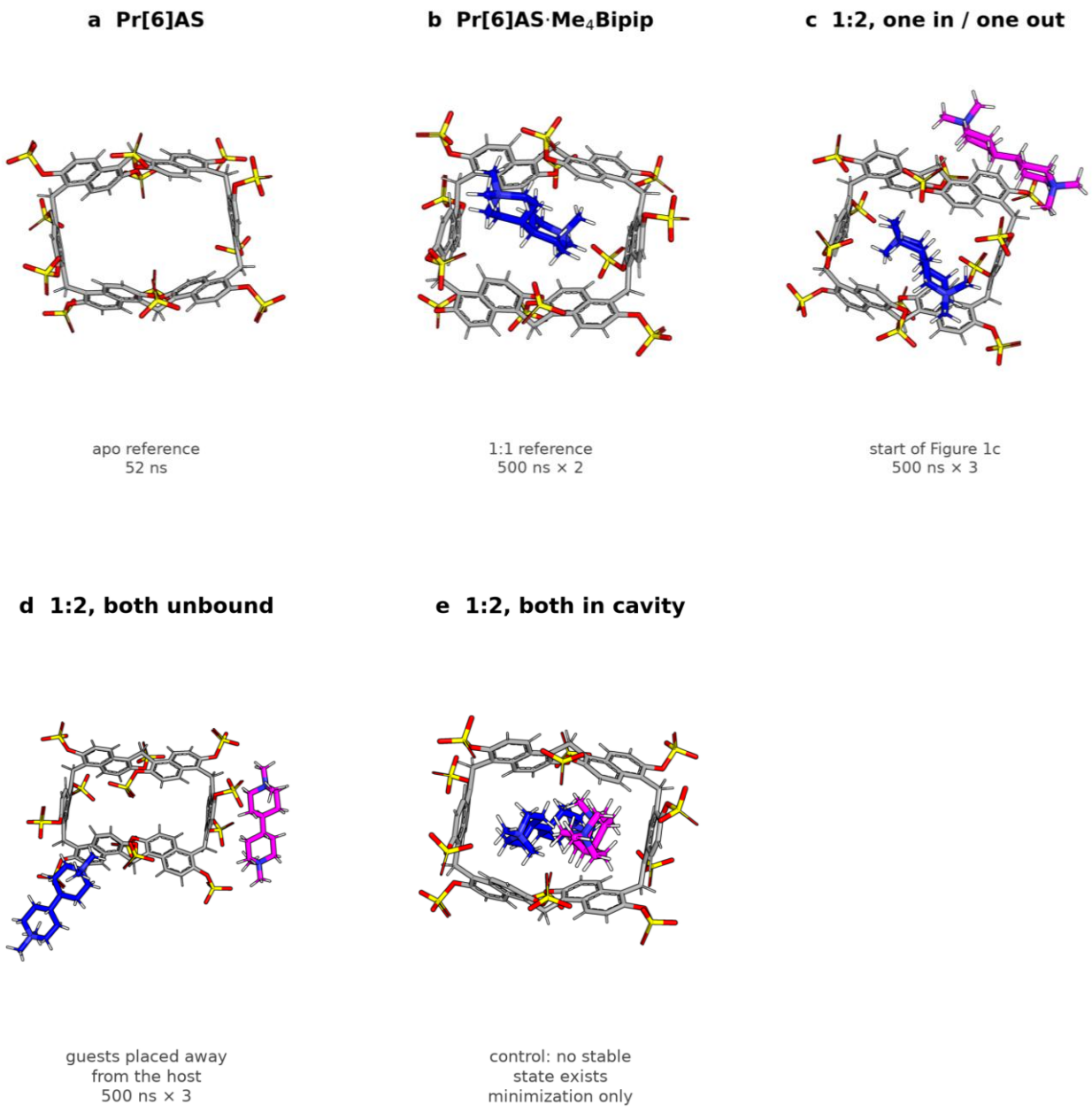


Figure S31. Starting configurations. a) Pr[6]AS alone. b) Pr[6]AS·**6q**, guest in the cavity. c) 1:2 with one **6q** in the cavity and one at the sulfated portal the geometry of Figure 1c, taken from the MMFF-optimized complex. d) 1:2 with both **6q** guests placed away from the host. e) 1:2 with both guests force-docked into the cavity (the geometry of Figure 1b, a control for which no stable force-field state exists). The two guests are colored blue and magenta. Water and ions are omitted.

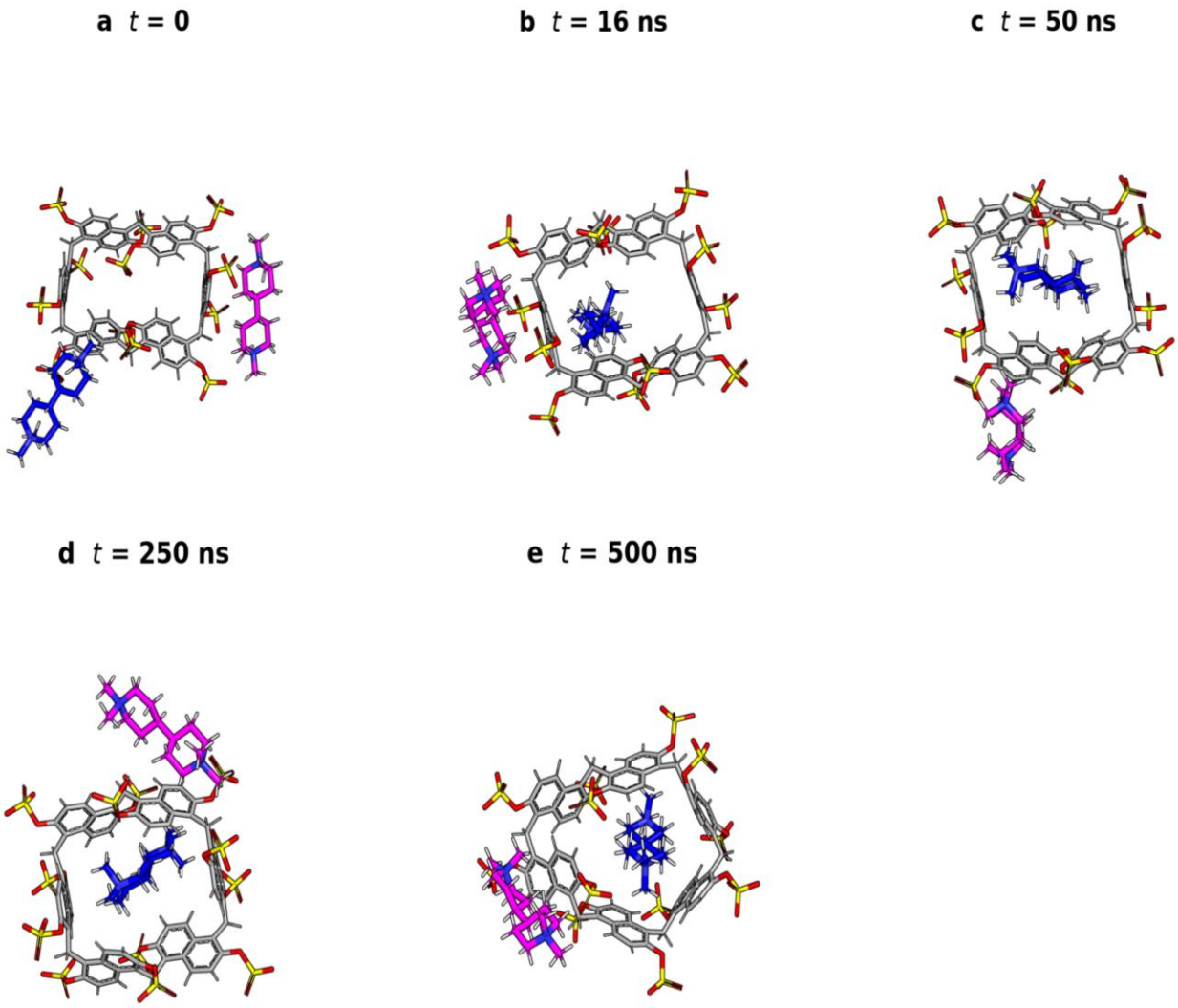


Figure S32. Snapshots from the 1:2 simulation started with both **6q** guests away from the host. a) The first production frame: both guests are already associated with the convex equatorial region of Pr[6]AS, at 10.3–11.4 Å from the host center of mass (the rim-bound mean is 10.1 Å); the migration from bulk happened during equilibration. b) t = 16 ns, the frame at which one guest threads the cavity. In b) and c) (t = 50 ns) the second guest lies against the exterior naphthalene wall in the geometry of Figure 1d, contacting three sulfates. d) t = 250 ns, the frame shown in SC2d, with the second guest.

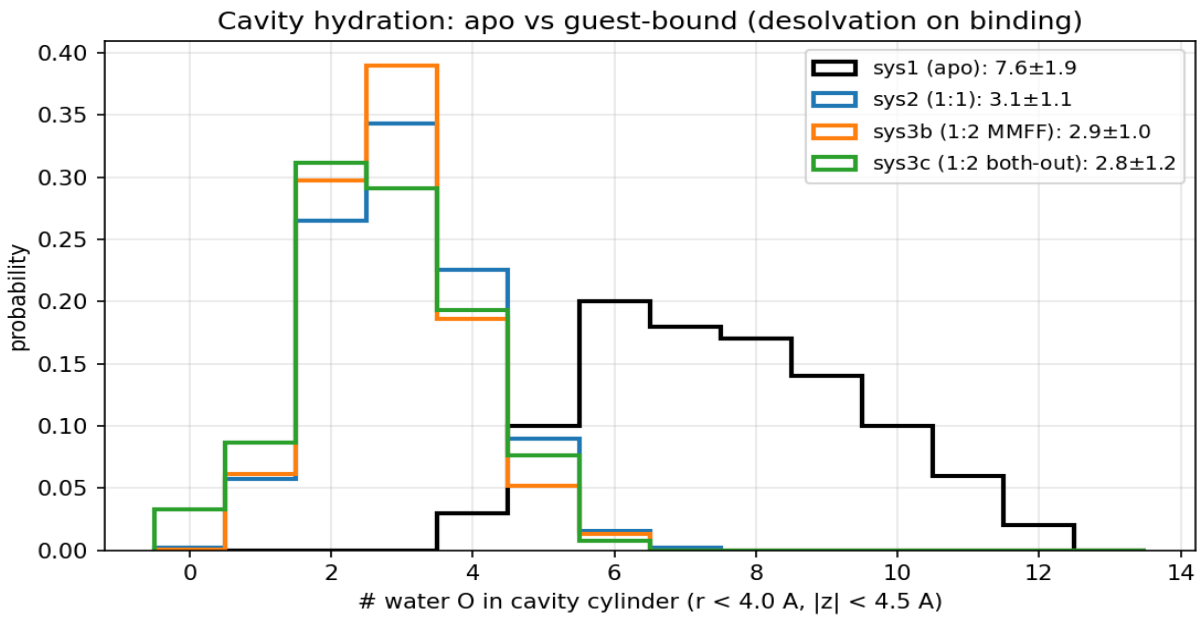


Figure S33. Distribution of the number of water molecules inside the cavity of Pr[6]AS for uncomplexed Pr[6]AS and the two guest-bound systems. Uncomplexed Pr[6]AS holds 7.6 ± 1.9 water molecules; Pr[6]AS·**6q** holds 3 ± 1.1, and the two 1:2 systems 3 ± 1.0 and 3 ± 1.2. Binding therefore expels approximately five water molecules, and the second guest expels none the change is complete after the first binding event.

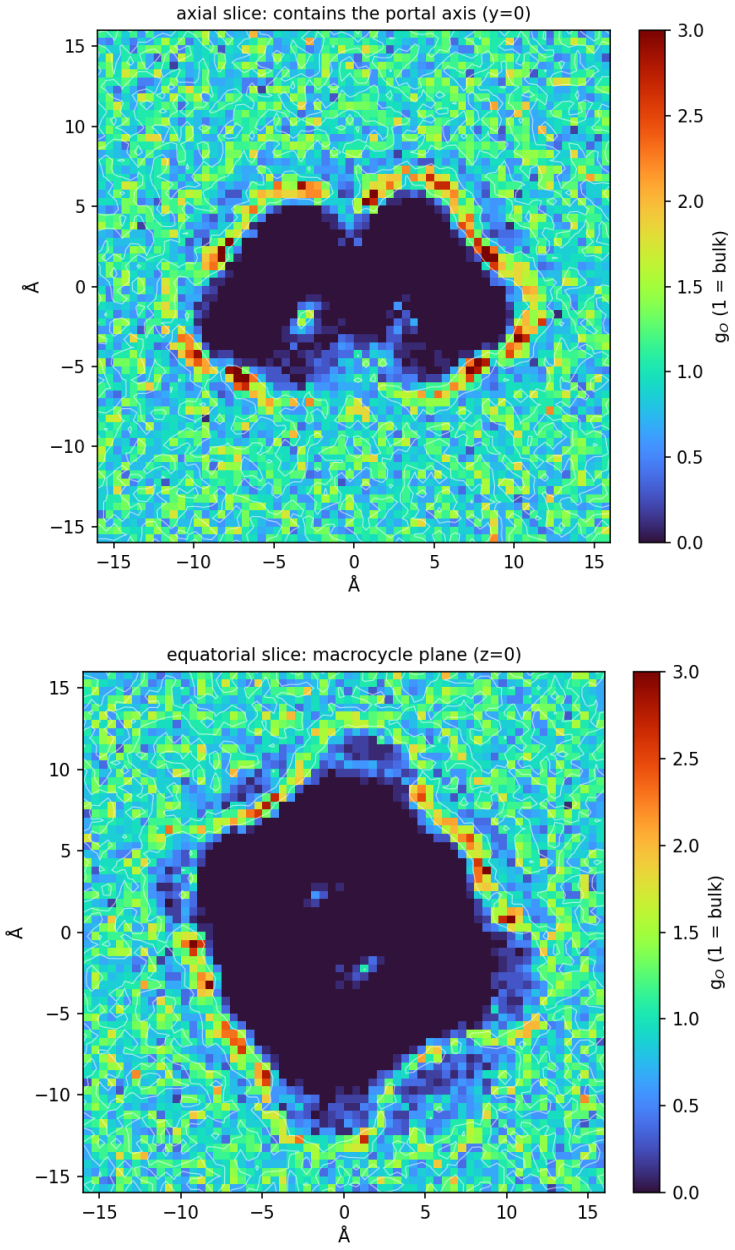


Figure S34. Water oxygen density g_O around Pr[6]AS·(**6q**)$_2$ in a reference frame fixed to the host, shown as an axial slice (containing the macrocycle normal) and an equatorial slice (perpendicular to it). Blue is depleted relative to bulk, red enriched. The cavity is desolvated to 19% of bulk density while the twelve sulfate groups retain discrete hydration shells at 2–3 times bulk density. Integrated over the cavity cylinder this is a 62% loss of cavity water against the uncomplexed host, versus a 7% loss of water around the sulfate groups (7.89 → 7.3 waters per sulfate): **6q** inserts into the pre-existing sulfate hydration shell rather than displacing it.

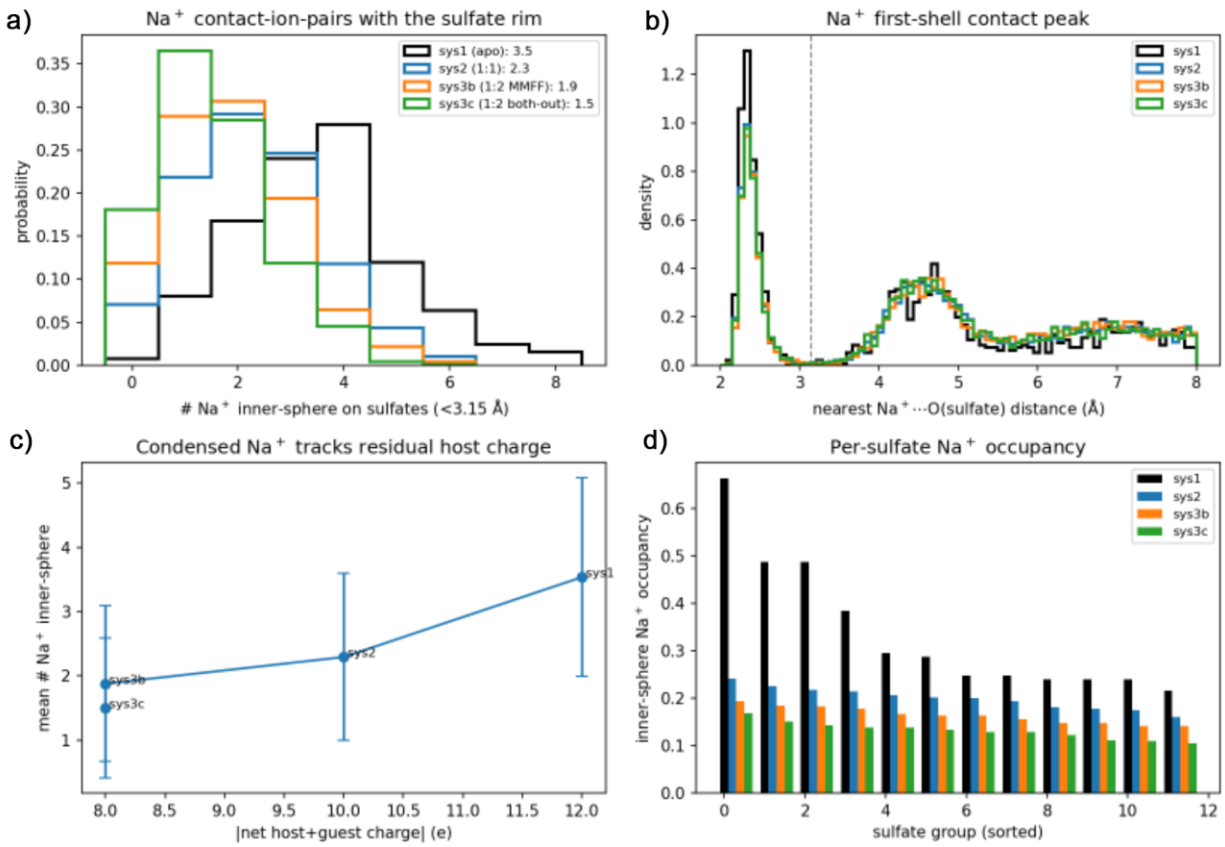


Figure S35. Na^+ coordination to the sulfate groups of Pr[6]AS. a) Distribution of the number of inner-sphere Na^+ contact ion pairs ($Na^+\cdots O$(sulfate) <3.15 Å): the mean falls from 3.5 for uncomplexed Pr[6]AS to 2.3 for Pr[6]AS·**6q** and to 1.9 and 1.5 for the two 1:2 systems. b) Distribution of the nearest $Na^+\cdots O$(sulfate) distance, peaking at 2.4 Å in every system; the dashed line marks the 3.15 Å inner-sphere cutoff. c) Mean inner-sphere Na^+ count against the residual net charge of the host–guest complex. d) Per-sulfate inner-sphere Na^+ occupancy. Uncomplexed Pr[6]AS additionally holds 0.98 Na^+ inside the cavity; this falls to 0.03 or below in all guest-bound systems.

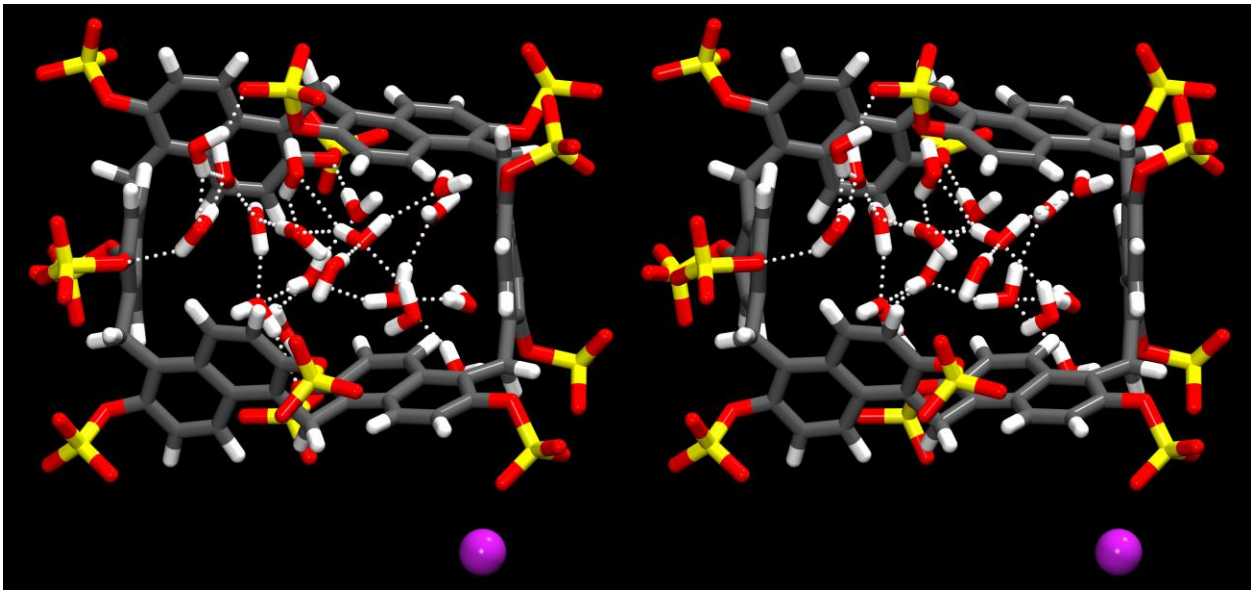


Figure S36. Cavity water of uncomplexed Pr[6]AS when no Na^+ is in the cavity, shown as a cross-eyed stereo pair. The snapshot is from apo replicate 2 at 137 mM NaCl and 298.15 K (t = 36.5 ns). It holds 9 cavity waters, the median count for frames without a cavity Na^+. The frames make up 8% of the trajectory frames (42 episodes across three replicates). In them, the cavity holds 9.5 waters that form 2.95 hydrogen bonds each, compared with 3.66 for bulk water. Only the cavity waters and the waters hydrogen-bonded to them are shown. White dotted lines are hydrogen bonds with a cavity water as donor or acceptor (donor–acceptor ≤3.5 Å, D–H···A ≥130°). The view is along the macrocycle axis, tilted by 25°. C, gray; O, red; S, yellow; H, white; Na^+, magenta (a contact ion pair at the rim).

Computational methods

Systems and initial conditions. The starting structures of the complexes were generated from a previously optimized Pr[6]AS·(Me_4Bipip)$_2$ structure via Spartan'24, using an MMFF94[S1] force field. One guest molecule occupied each of the sulfated portals. Using RDKit, all the hydrogen atoms were retained. The guest that was closest to the host's center-of-mass was selected as the cavity guest. Four systems were created from Spartan'24 Pr[6]AS·(Me_4Bipip)$_2$ structure: (i) Pr[6]AS with no guest molecules present; (ii) Pr[6]AS with only one guest molecule, Me_4Bipip, occupying the central binding site; (iii) Pr[6]AS with both Me_4Bipip guest molecules located either inside the binding pocket (as shown in Figure 1C) and outside it at one of the sulfated portals ("one-in/one-out"); and (iv) Pr[6]AS with both Me_4Bipip guest molecules randomly placed in solution ("both-unbound") approximately 22 and 43 Å away from the host center-of-mass after energy minimization. Each of these four systems was simulated at 300 K and with 137mM NaCl for 3 × 100 ns, 3 × 100 ns, 3 × 500 ns and 3 × 500 ns.

Force field. Host and guest molecules were parameterized as an OpenFF Sage 2.3.0 [S2,S3] (openff_unconstrained-2.3.0.offxml) using the OpenFF Toolkit 0.18.0 and OpenFF Interchange 0.5.2. Guest charges were computed with AM1-BCC[S4,S5] (sqm, AmberTools 24.8 [S6], via the OpenFF Toolkit) on a single RDKit-generated conformer with antechamber's default AM1 geometry optimization. Host charges were assigned with OpenFF NAGL model openff-gnn-am1bcc-1.0.0 (NAGL 0.5.4) [S7]. Water was modeled with TIP3P [S8] and Na^+ and Cl^- with Joung–Chatham parameters [S9], with salt concentration set to 137 mM.

Simulation settings. Simulations used OpenMM 8.4 [S10] (CUDA platform, mixed precision). Electrostatics: particle-mesh Ewald [S11,S12], 0.9 nm real-space cutoff, error tolerance 10^{-4}. Lennard–Jones: 0.9 nm cutoff with switching from 0.8 nm and a long-range dispersion correction. Water was rigid; host and guest bonds were flexible with standard hydrogen masses. Integrator: Langevin middle [S13], friction 1 ps^{-1}, 300 K (298.15 K for the 137 mM runs). Barostat: Monte Carlo [S14,S15], 1 atm, isotropic, every 25 steps.

Relaxation and production. Each system was minimized with L-BFGS[S16] (up to 10,000 iterations; tolerance 10 kJ mol^{-1} nm^{-1}), assigned Maxwell–Boltzmann velocities at the simulation

temperature, and equilibrated in three stages: 100 ps NVT, 1 fs step, 500 ps NPT, 2 fs step and a 2 ns unrestrained NPT, 2 fs step. The first two stages used a 1000 kJ mol^{-1} nm^{-2} position restraints on host and guest heavy atoms. Production runs were unrestrained NPT with a 2 fs step, run as three replicates 100ns (i, ii) and 500ns (iii, iv). The coordinates were saved every 20 ps and energies every 100 ps. Replicates of systems (i)–(iv) started from the same equilibrated structure with new velocities and random seeds.

Analysis. Trajectories were analyzed with MDTraj 1.11 [S17] and MDAnalysis 2.10 [S18,S19] using the minimum-image distance convention. The first 10 ns of each 1:1 and one-in/one-out trajectory were discarded as equilibration; in the both-unbound trajectories, the frames before the guest entered the cavity were discarded, and the apo trajectories were used in full. The analyses are implemented in prism6md, a small Python package built on MDAnalysis and included in the Zenodo deposit (see Software and data). Given a topology and trajectory, prism6md identifies the host, guests, water and ions from their bonded fragments. In every frame, it places the host in a reference frame centered on the host's center of mass, with z along the macrocycle normal. Within that frame, it computes per-frame host shape, guest position and orientation, cavity hydration, and counterion contacts, and reports the averages quoted in the text.

Host frame. The guest positions were measured relative to the host, with the origin at the host center of mass and the *z* axis $\mathbf{e}_z$ normal to the macrocycle ring. In each snapshot $\mathbf{e}_z$ was taken as the direction in which the twelve sulfur atoms are least spread (from the host's inertia tensor). For a guest whose center of mass is displaced by **d** from the host center of mass,

$$z = \mathbf{d}\cdot\mathbf{e}_z,\ r = |\mathbf{d} - z\mathbf{e}_z| \quad \text{(S1)}$$

and θ is the angle between the guest's N→N vector and $\mathbf{e}_z$ (0–90°). A guest is in the cavity when its center of mass is within 4 Å of the host center of mass.

Host geometry. To measure the size and shape of the host, we computed four quantities in each snapshot. The overall size was measured by the radius of gyration, mass-weighted over all host atoms. The spacing between sulfate groups were measured by two the S···S distances. The d_{adj} was between sulfates on adjacent panels at the same portal (12 pairs) and the d_{opp} is between the two

sulfates of one panel (6 pairs). Eccentricity measures how far the ring departs from a circle, computed separately for the 12 sulfur atoms and for the 6 bridging CH_2 carbons:

$$e = (1 - \lambda_2/\lambda_1)^{1/2} \quad \text{(S2)}$$

Where $\lambda_1 \geqslant \lambda_2$ are the eigenvalues of the in-plan gyration tensor of those atoms ($e = 0$ for a circle, approaching 1 for a flattened ellipse). The radial position of each sulfate was measured as the perpendicular distance of its sulfur atom from the host axis.

Hydration. To quantify how many waters occupy the cavity and the remaining hydration is arranged around the host we computed three measurements. Cavity waters were counted as the water oxygens inside. A cylinder coaxial with host frame with $r < 4.0$ Å and $|z| < 4.5$ Å, sampled every 100 ps. To identify waters that link the guest to the sulfates a bridging water was defined as one within 4.5 Å of a guest N and within 3.5 Å of a terminal sulfate O (an O within 1.8 Å of S and not within 1.7 Å of C). To map where water is gained or lost around the host, three-dimensional water densities were computed after aligning each frame on the host heavy atoms with $\mathbf{e}_z$ along z, on a 0.5 Å grid.

Cavity-water hydrogen bonds. To test whether cavity water is under-coordinated relative to bulk, as expected for high-energy water we counted hydrogen bonds for each cavity water using the criterion of Biedermann et al. [S20] (D···A ≤ 3.5 Å, D–H···A ≥ 130°). Bonds to other waters were counted and so were bonds donated to terminal sulfate O, aryl ester O and Cl^- (≤ 3.85 Å); Na^+ contacts are not counted as hydrogen bonds. The criterion of Wernet et al. [S21] was used as a check. For comparison, bulk water was defined as water more than 12 Å from all solute heavy atoms (m_bulk = 3.66). To compare with the hosts in ref. S20, the hydrogen-bond deficit of the cavity was summarized as

$$Z = N\,(3.62 - m) \quad \text{(S3)}$$

with N the mean number of cavity waters, m their mean hydrogen-bond count, and 3.62 the bulk value of ref. S20. Statistics were computed for all frames and separately for frames with no Na^+ in the cavity; consecutive Na^+-free frames were grouped.

Software and data. OpenMM 8.4; OpenFF Toolkit 0.18.0, Interchange 0.5.2, NAGL 0.5.4; Sage 2.3.0; AmberTools 24.8; RDKit 2025.09.5; PACKMOL 20.14.3[S22]; MDTraj 1.11; MDAnalysis

2.10; NumPy 2.4.3[S23]; SciPy 1.17.1[S24]; PyMOL. The Zenodo deposit (https://zenodo.org/records/21999927) contains the starting structures and charged molecules; for every system, the parametrized OpenMM system, the solvated and equilibrated coordinates, and the equilibration and production logs; the setup, equilibration, and production scripts used for the 137 mM systems, with a conda environment file. It also contains prism6md, a Python package built on MDAnalysis that computes the MD quantities reported in the main text, with its output for every production trajectory; the deposit README lists the prism6md command that computes each reported quantity.

References

[S1] Halgren, T. A. *J. Comput. Chem.* **1996**, *17*, 490–519.

[S2] Mobley, D. L.; Bannan, C. C.; Rizzi, A.; Bayly, C. I.; Chodera, J. D.; Lim, V. T.; Lim, N. M.; Beauchamp, K. A.; Slochower, D. R.; Shirts, M. R.; Gilson, M. K.; Eastman, P. K. *J. Chem. Theory Comput.* **2018**, *14*, 6076–6092.

[S3] Boothroyd, S.; Behera, P. K.; Madin, O. C.; Hahn, D. F.; Jang, H.; Gapsys, V.; Wagner, J. R.; Horton, J. T.; Dotson, D. L.; Thompson, M. W.; Maat, J.; Gokey, T.; Wang, L.-P.; Cole, D. J.; Gilson, M. K.; Chodera, J. D.; Bayly, C. I.; Shirts, M. R.; Mobley, D. L. *J. Chem. Theory Comput.* **2023**, *19*, 3251–3275.

[S4] Jakalian, A.; Bush, B. L.; Jack, D. B.; Bayly, C. I. *J. Comput. Chem.* **2000**, *21*, 132–146.

[S5] Jakalian, A.; Jack, D. B.; Bayly, C. I. *J. Comput. Chem.* **2002**, *23*, 1623–1641.

[S6] Case, D. A.; et al. *AmberTools 24*; University of California: San Francisco, 2024.

[S7] Open Force Field Initiative. OpenFF NAGL: Neural Network Approach to Generate Atomic-Level Charges, model openff-gnn-am1bcc-1.0.0. https://docs.openforcefield.org/projects/nagl/ (accessed August 19, 2026).

[S8] Jorgensen, W. L.; Chandrasekhar, J.; Madura, J. D.; Impey, R. W.; Klein, M. L. *J. Chem. Phys.* **1983**, *79*, 926–935.

[S9] Joung, I. S.; Cheatham, T. E., III. *J. Phys. Chem. B* **2008**, *112*, 9020–9041.

[S10] Eastman, P.; Galvelis, R.; Peláez, R. P.; Abreu, C. R. A.; Farr, S. E.; Gallicchio, E.; Gorenko, A.; Henry, M. M.; Hu, F.; Huang, J.; Krämer, A.; Michel, J.; Mitchell, J. A.; Pande, V. S.; Rodrigues, J. P. G. L. M.; Rodriguez-Guerra, J.; Simmonett, A. C.; Singh, S.; Swails, J.; Turner, P.; Wang, Y.; Zhang, I.; Chodera, J. D.; De Fabritiis, G.; Markland, T. E. *J. Phys. Chem. B* **2024**, *128*, 109–116.

[S11] Darden, T.; York, D.; Pedersen, L. *J. Chem. Phys.* **1993**, *98*, 10089–10092.

[S12] Essmann, U.; Perera, L.; Berkowitz, M. L.; Darden, T.; Lee, H.; Pedersen, L. G. *J. Chem. Phys.* **1995**, *103*, 8577–8593.

[S13] Zhang, Z.; Liu, X.; Yan, K.; Tuckerman, M. E.; Liu, J. *J. Phys. Chem. A* **2019**, *123*, 6056–6079.

[S14] Chow, K.-H.; Ferguson, D. M. *Comput. Phys. Commun.* **1995**, *91*, 283–289.

[S15] Åqvist, J.; Wennerström, P.; Nervall, M.; Bjelic, S.; Brandsdal, B. O. *Chem. Phys. Lett.* **2004**, *384*, 288–294.

[S16] Liu, D. C.; Nocedal, J. *Math. Program.* **1989**, *45*, 503–528.

[S17] McGibbon, R. T.; Beauchamp, K. A.; Harrigan, M. P.; Klein, C.; Swails, J. M.; Hernández, C. X.; Schwantes, C. R.; Wang, L.-P.; Lane, T. J.; Pande, V. S. *Biophys. J.* **2015**, *109*, 1528–1532.

[S18] Michaud-Agrawal, N.; Denning, E. J.; Woolf, T. B.; Beckstein, O. *J. Comput. Chem.* **2011**, *32*, 2319–2327.

[S19] Gowers, R. J.; Linke, M.; Barnoud, J.; Reddy, T. J. E.; Melo, M. N.; Seyler, S. L.; Domański, J.; Dotson, D. L.; Buchoux, S.; Kenney, I. M.; Beckstein, O. In *Proceedings of the 15th Python in Science Conference*; Benthall, S., Rostrup, S., Eds.; 2016; pp 98–105.

[S20] Biedermann, F.; Nau, W. M.; Schneider, H.-J. *Angew. Chem., Int. Ed.* **2014**, *53*, 11158–11171.

[S21] Wernet, P.; Nordlund, D.; Bergmann, U.; Cavalleri, M.; Odelius, M.; Ogasawara, H.; Näslund, L. Å.; Hirsch, T. K.; Ojamäe, L.; Glatzel, P.; Pettersson, L. G. M.; Nilsson, A. *Science* **2004**, *304*, 995–999.

[S22] Martínez, L.; Andrade, R.; Birgin, E. G.; Martínez, J. M. *J. Comput. Chem.* **2009**, *30*, 2157–2164.

[S23] Harris, C. R.; Millman, K. J.; van der Walt, S. J.; Gommers, R.; Virtanen, P.; Cournapeau, D.; Wieser, E.; Taylor, J.; Berg, S.; Smith, N. J.; Kern, R.; Picus, M.; Hoyer, S.; van Kerkwijk, M. H.; Brett, M.; Haldane, A.; Fernández del Río, J.; Wiebe, M.; Peterson, P.; Gérard-Marchant, P.; Sheppard, K.; Reddy, T.; Weckesser, W.; Abbasi, H.; Gohlke, C.; Oliphant, T. E. *Nature* **2020**, *585*, 357–362.

[S24] Virtanen, P.; Gommers, R.; Oliphant, T. E.; Haberland, M.; Reddy, T.; Cournapeau, D.; Burovski, E.; Peterson, P.; Weckesser, W.; Bright, J.; van der Walt, S. J.; Brett, M.; Wilson, J.; Millman, K. J.; Mayorov, N.; Nelson, A. R. J.; Jones, E.; Kern, R.; Larson, E.; Carey, C. J.; Polat, İ.; Feng, Y.; Moore, E. W.; VanderPlas, J.; Laxalde, D.; Perktold, J.; Cimrman, R.; Henriksen, I.; Quintero, E. A.; Harris, C. R.; Archibald, A. M.; Ribeiro, A. H.; Pedregosa, F.; van Mulbregt, P.; SciPy 1.0 Contributors. *Nat. Methods* **2020**, *17*, 261–272.